University of Alberta

Three-scale modeling and numerical simulations of fabric materials

By

Weijie Xia

A thesis submitted to the Faculty of Graduate Studies and Research
in partial fulfillment of the requirements for the degree of
Doctor of Philosophy

in

Mechanical Engineering

Spring 2011
Edmonton, Alberta

Examining Committee

Ben Nadler, Mechanical Engineering

Chongqing Ru, Mechanical Engineering

Peter Schiavone, Mechanical Engineering

Samer M. Adeeb, Civil Engineering

Tian Tang, Mechanical Engineering

Luis Dorfmann, Civil and Environmental Engineering, Tufts University

Abstract

Based on the underlying structure of fabric materials, a three-scale model is constructed to describe the mechanical behavior of fabric materials. The current model assumes that fabric materials take on an overall behavior of anisotropic membranes, so membrane scale is taken as the macroscopic or continuum scale of the model. Following the membrane scale, yarn scale is introduced, in which yarns and their weaving structure are accounted for explicitly and the yarns are modeled as extensible elasticae. A unit cell consisting of two overlapping yarns is used to formulate the weaving patterns of yarns, which governs the constitutive nonlinear behavior of fabric materials. The third scale, named fibril scale, zooms to the fibrils inside a yarn and incorporates its material properties. Via a coupling process between these three scales, the overall behavior and performance of the complex fabric products become predictable by knowing the material properties of a single fibril and the weaving structure of the fabrics. In addition, potential damage during deformation is also captured in the current model through tracking the deformation of yarns in fibril scale.

Based on the multi-scale model, both static and dynamic simulations were implemented. Comparison between the static simulations and experiment demonstrates the model abilities as desired. Through the dynamic simulations, parameter research was conducted and indicates the ballistic performance and mechanical behavior of the fabric materials are determined by a combination of various factors and conditions rather than the material properties alone. Factors such as boundary conditions, material orientation and projectile shapes etc. affect the damage patterns and energy absorption of the fabric.

Keywords: fabric; multiscale; damage; impact; modeling; armor; ballistic

Acknowledgment

I would like to thank my supervisor, Dr. Ben Nadler, for his patient and friendly instruction during my study and research work with him. I really appreciate the way he teaches because he always explains profound theories in simple words and examples and also extends his answers to related knowledge. This is the invaluable way to broaden my vision of learning. I also want to thank Dr. Peter Schiavone for his support and encouragement when I came into difficulties with my studies. To Dr. Samer Adeeb, I appreciate his generous help providing me access to the simulation software despite the license resource is quite limited. Thanks also for his guidance and help with the simulation work.

Table of Contents

List of Tables

List of Figures

Nomenclature

$\mathbf{F}$	Membrane deformation gradient
$\boldsymbol{l}_i$	Base vectors of deformed configuration
$\boldsymbol{L}_i$	Base vectors of referential configuration
$i = 1, 2$	Subscription indicating warp and fill yarns (or yarn directions)
λ_i	Membrane stretch in $\boldsymbol{l}_i$ directions
$\mathbf{E}$	Membrane Lagrangian strain tensor
E_i	Membrane Lagrangian strain in $\mathbf{L}_i$ directions
$\mathbf{P}$	Piola-Kirchhoff stress tensor
P_i	Piola-Kirchhoff stress (force/length) in $\boldsymbol{L}_i$ directions
A	Stretch stiffness of the yarn
A^0	Stretch stiffness of undamaged yarn
B	Bending stiffness of the yarn
B^0	Bending stiffness of undamaged yarn
δ	Local elastica extension
γ	Bending strain of the elastica
S, s	Parameter of the length or location along the elastica (yarn) in the referential and deformed configurations
M	Bending moment
N	Yarn internal axial tensile force
Q	Yarn internal shearing force
μ	Local stretch of the elastica (yarn)
$\mu^{h.max}$	History maximum local stretch of the elastica (yan)

F_i	Applied external force on the yarn
V	Inter-yarn contact force
ε_i	Lagrangian strain of the yarn
d_0	Transverse dimension of the yarn
d_j	Misalignment of individual fibril
U_j	Stretch of individual fibril
E_I^*	Effective modulus of the yarn
E_I	Elastic modulus of a fibril
U_{crit}	Critical stretch of the fibril
α_i	Damage parameters defining the yarn damage
β	Parameter reflecting the degree of fibril misalignment
u_i	Tangential displacement of the yarns at contact point
w_i	Half length of the unit cell
C	Yarn cross-section area
$\Phi,\ \phi$	Yarn weaving angles in referential and deformed configurations
Y0	Two-edge fixed in Y direction and material orientated at 0°
XY45	Four-edge fixed and material orientated at 45°
XY0	Four-edge fixed and material orientated at 0°
SDV1	Damage status parameter, evaluated as 0 only if the fabric is completely damaged in both warp and fill yarn directions, otherwise evaluated as 1.
SDV2	SDV2 = α_1, the damage status parameter in warp yarns
SDV3	SDV3 = $\alpha_{2,}$ the damage status parameter in fill yarns

Chapter 1

Introduction

1.1 Objective and work outline

With technology developing, greatly improved high strength fabric materials are becoming more and more attractive because of their high strength-to-weight ratio, like Zylon and Kevlar. The high strength fabric materials are extensively applied in modern industries such as bullet-proof vest, aviation craft protective layers against high-speed projectiles. They can also be frequently found in various fields where high strength and light-weighted flexible materials are desired like sport equipment and boat sails.

In order to have an effective and safe application of these fibrous materials, a demand of an accurate and practical model arises to predict the fabric behavior and for design optimization. The purpose of this work is to develop a multi-scale fabric material model which is able to:

(1) track possible damage in the fabric;

(2) reflect the yarn weaving structures;

(3) capture the yarn-to-yarn interaction.

The multi-scale approach is chosen to model the fabric materials, because the modeling work is split into parts (scales). In each scale, proper theories or techniques can be employed to describe one or more types of particular nature of the fabric materials. The current fabric material model introduces three scales based on the structural hierarch of the fabric materials.

Following the material modeling work, dynamic and static numerical simulations are implemented with the three-scale material model.

The simulated results are demonstrated and compared with experimental work to inspect the model abilities and accuracy. Further study on fabric ballistic performance and parameter research was also conducted via the dynamic simulations. The findings obtained from the dynamic research can be referred to improve the ballistic performance of the fabric.

Static simulations are uniquely valuable as some constitutive nature or behavior of the material can hardly be observed or noticed in dynamic simulations. At static status, the material behavior is completely determined by its constitutive nature and distractions from dynamic factors are removed. The static simulations are implemented under various loading conditions to investigate the fabric response. The simulations are compared with experiments from other studies for verification and the results demonstrate the model abilities as desired.

1.2 Literature review

In the past decades, various research and modeling work has been done with different experimental techniques or mathematic formulations or in a combined approach to study and predict the behavior of the fabric materials.

Early work on fabric materials used continuum models or the traditional empirical approach. Continuum models consider the fabric materials as continuum materials and formulate them by utilizing continuum mechanics tools. Material property parameters are defined to derive governing equations. Examples of this approach include work by Vinson and Zukas [1], Phoenix and Porwal [2], Gu [3] and Billon and Robinson[4]. Since the continuum models ignore the sub-structure or micro structure of the fabric materials, it may not provide satisfactory prediction for some physical phenomena due to the weaving structure of the fabric materials. However, this research approach built a solid base for further development in mathematical modeling research of fabric materials. Empirical techniques are also utilized in the modeling research of fabric materials. The material behaviors are analyzed through experimental data and build up the constitutive law, for example [5, 6, 7, 8]. Sophisticated mathematic tools such as curve fitting and statistical analysis are often used to process experimental data. The results mainly remain valid and accurate for a particular type or class of materials.

For the fabric materials, their behaviors are greatly affected by the yarn weaving structures as opposite to the continuum membrane. Thus, continuum models should not be sufficient due to the ignorance of the underlying micro-structure. Researchers realized the importance and then introduced various techniques to capture the sub-structure features of fabric materials. One of the techniques is the network model which simplifies the yarn weaving structure as a network of pin-jointed bar members. Shim et al. [9] modeled the network as spring and dashpot structure using a three-element viscoelastic model. Zohdi et al [10] idealized the woven-yarns as a pin-pointed truss and the network is composed of flexible bar segments. However, the network models lose the ability of describing inter-yarn movement because the interaction of woven yarn is simplified to pin-jointed nodal points to form a network system. The network models ignore the weaving geometry, inter-yarn sliding, friction and coupling effects. Therefore it is not able to model yarn decrimping. Whereas, at the early stage of fabric material deformation, yarn decrimping is the dominate characteristic of fabric materials and accounts for the major part of fabric deformation. Ivanov and Tabiei [11] considered the weaving structures. In [11], the yarns are simplified as pin-jointed straight viscoelastic bars connected with a rigid link at the crossover (interaction) points between warp and fill yarns. Fabric shearing resistance is considered through yarn rotational friction. More advanced models [12, 13] model the yarns as piecewise rigid rods connected with springs. The yarns are represented as a network of trusses connected by pin-joints at their crossover points. The rigid bars are connected with bending springs. The yarns in contact at the crossover points are connected with torsion springs.

Multi-scale approach is a more advanced modeling technique, which views the fabric materials in different scales corresponding to their natural structure hierarchy. When observed in macro- or micro-scopic scales, the fabric materials take on completely different architectures and properties. For each scales, proper theories and assumptions are applied. Therefore, the multi-scale approach provides a flexible way to adopt advantages of other approaches. More advanced and accurate material models are expected from this approach since it considers both the overall characteristic of the materials and any sub-scopic nature of the materials. Nadler et al. [14] introduced two scales to the model the fabric materials, namely membrane scale and yarn scale. The membrane scale accounts for the overall membrane-like nature of the fabric materials. The yarn scale capture the weaving structure, yarn geometry and yarn interaction so that the substructure-induced properties can be reflected. Zohdi and Powell [10] employed a truss structure to describe the fabric materials and considered fibril misalignment in the yarns. a damage criterion is developed by monitoring the yarn stretch through statistical computation.

Modeling of inter-yarn friction and movement is a challenging work. A few researchers [15, 16] developed computational models taking into account the inter-yarn frictional sliding and the yarn crimp and weaving structure. In [15], it is found that the ballistic response of woven fabric is very sensitive to yarn friction when the friction coefficient is within a certain range and greatly affect absorption of impact energy. The numerical model in [16] simulates the transverse yarn interaction and the results indicate that crimping, decrimping, and yarn-yarn interaction have a significant effect on ballistic response models.

In recent years, numerical modeling becomes more and more popular because of advances in computation technology. The numerical modeling work utilizes the finite element software packages ABAQUS, LSDYNA and ANSYS. In addition to the commercial packages, there are also open source versions developed specially for academic purposes. Commercial packages usually are more powerful in handling contact, loading conditions, complex geometries and assembly. Some researchers are in favor of academic packages of finite element software since they are completely open source. With the finite element analysis tools, the yarn structures are modeled explicitly in elements. Johnson et al. [17] modeled the fabric as a combination of bar members and thin membrane. The bar elements represent the yarns and the membrane elements renders shear resistance and the overall structural properties of the fabric. Lim et al. [15] modeled the fabric material with membrane elements in DYNA3D and defined viscoelasticity of the fabric. Damage criterion is also defined through the strain level of the fabric and the critical strain is a function of strain rate. At high strain rate, the critical strain level is significantly reduced. However, since the model considers the fabric material as continuum membrane, the yarn-to-yarn interaction was neglected.

Zeng et al. [18] considered the inter-yarn friction, yarn crimp, viscoelasticity and inter-yarn sliding. In [18], friction was studied to investigate its influence on energy absorption and on the ballistic performance of the fabric. The results show that the ballistic response is sensitive to the friction within a low level range and high level friction leads to premature damage and thus reduces energy absorption. Duan et al. [19, 20, 21] investigated the influences of friction level and boundary conditions on energy absorption. In their modeling work, the inter-yarn friction and projectile-fabric friction range from 0 to 0.5 and the modeling results show the friction delays fabric failure and increases energy absorption. Investigation on boundary conditions shows the two edge clamped situation absorbs more energy than four edge clamped condition. Shockey et al [22, 23,, 24, 25, 26] implemented a series of experimental tests and simulated the behaviors of single yarns and fabric corresponding to their experimental work. As one advantage, numerical models provides an easy way to fulfill realistic constraint conditions in the simulations such as inter-yarn sliding and inter-yarn friction, while it may cause great difficulties in mathematical modeling work. However, numerical models can be computationally costly because it involves a large number of freedom and inter-yarn contact sites.

1.3 Introduction of current work

In the following work, a multi-scale model of fabric materials is first developed, with which static and dynamic numerical simulations are implemented.

In the current work, the fabric materials under consideration are composed of a simple weaving structure of yarns. A yarn is composed of a large number of thin fibrils. The mechanical properties of the fibrils govern the mechanical property of the yarns in the micro-scale which in turn constitutes the mechanical property of the fabric in the macro-scale. So the fabric materials are studied on three different scales, membrane scale, yarn scale and fibril scale. For each scale, different governing equations describe the material nature of the corresponding scale. The material property and failure of the fabrics is described in the fibril scale through defining the fibril property.

Static simulations are implemented with MATLAB under various loading conditions. The results demonstrate the model can properly predict yarn decrimping, yarn interaction and gradual damage. Dynamic simulations are implemented with ABAQUS. Through the dynamic simulations, results from parameter research demonstrate the ballistic performance of the fabric is determined by a combination of a system of factors. Basically, these influence factors include the fabric boundary conditions, material orientation and projectile shapes.

Because the current simulation work is based on the multi-scale material model which considers the weaving structure and yarn interaction, the fabric is simply modeled as a piece of membrane when finite element analysis is implemented.

This significantly reduces the computational cost in contrast to numerical modeling work that usually involves a large number of solid elements and contact sites between yarns. In addition, based on the multi-scale material model, investigation on fabric of different structures and materials can be achieved by adjusting only the relevant parameters inside the code of the multi-scale material model.

The current simulation work considered influence factors extensively, including the boundary conditions, impact velocities, projectile shapes and friction between the projectile and the fabric. In the simulations, the finite element analysis model configuration follows exactly the same as experimental work. The material properties and structure information of the fabric were defined according to published data. The results agree with experimental work and the same conclusions were obtained as from numerical modeling work. Meanwhile, since more comprehensive investigation was conducted in the current work, more generalized conclusions were obtained.

Chapter 2

Basic theories and three-scale modeling[1]

In the current work, a three-scale model is considered and constructed based on the underlying structure of a fabric, as demonstrated in the following microscopic photos (Figure 2-1). The fabrics considered here are simply woven fabrics consisting of warp and fill yarns which are interlaced together. The names “warp” and “fill” indicate the distinction between the two types of yarns (or yarn directions) due to the manufacturing process. Warp yarns are usually crimped in a higher degree than the fill yarns and are less stiff. The degree of crimp is a measure of the elongation of a yarn when it is extracted and straightened. The degree of crimp has significant influences on the mechanical performance of the yarn. The anisotropy response of a fabric depends on the different stiffness and crimp of the yarns.

[1] A version of this chapter has been accepted for publication. International Journal of Engineering Science.

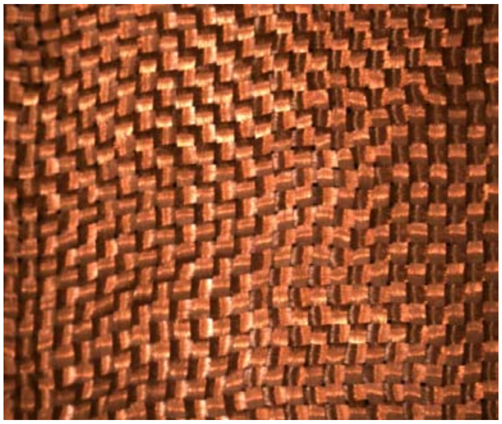

(a) membrane scale

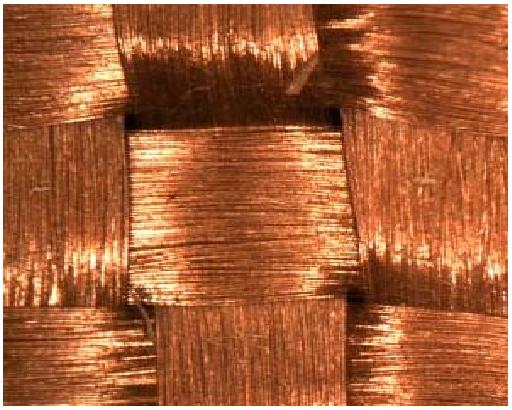

(b) yarn scale

(c) fibril scale

Figure 2-1 Microscopic photos of PBO Zylon showing the fabric structure in three scales

2.1 Membrane scale

Observed from distance, a fabric is a configuration of a continuum and smooth surface (Figure 2-1 (a)) with negligible bending stiffness. Therefore, as the first scale level, the fabric is modeled as a membrane. Two unit-vector fields $\mathbf{l}_i$ and $\mathbf{L}_i$ are introduced (Figure 2-2), which span the tangent plane of the membrane and are chosen to be aligned with the projection of corresponding yarns on the tangent plane.

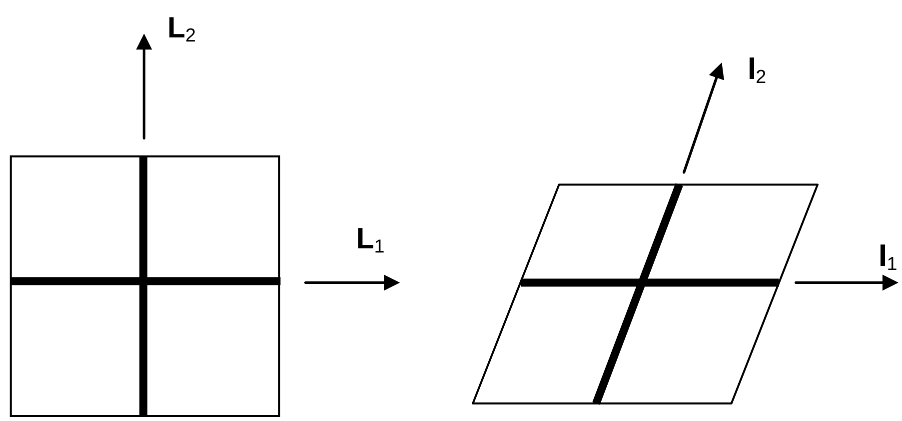

(a) Reference configuration (b) Deformed configuration

Figure 2-2 Description of yarn projection onto the tangent plane

The warp and fill yarns are chosen to be initially orthogonal in the reference configuration [14], i.e. $\mathbf{L}_1 \bullet \mathbf{L}_2 = 0$, such that the deformation gradient of the membrane is expressed as

$$\mathbf{F} = \lambda_1 \mathbf{l}_1 \otimes \mathbf{L}_1 + \lambda_1 \mathbf{l}_2 \otimes \mathbf{L}_2 , \tag{2-1}$$

where $\mathbf{F}$ is the deformation gradient, $\mathbf{l}_i$ and $\mathbf{L}_i$ ($i = 1, 2$) are the two sets of unit vector fields in the deformed and referential configurations of the membrane, and λ_i are the associated stretches in $\mathbf{l}_i$ directions. $\mathbf{l}_i$ are chosen to be aligned with the projection of the yarns on the tangent plane in the deformed configuration. The subscripts $i = 1, 2$ denotes the directions of warp and fill yarns respectively and this convention applies throughout this work. Based on the definition of deformation gradient (Eqn. (2-1)), the Lagrangian strain tensor (membrane strain) is defined as

$$\mathbf{E} = \frac{1}{2}\left[\left(\lambda_1^{\,2} - 1\right)\mathbf{L_1} \otimes \mathbf{L_1} + \left(\lambda_2^{\,2} - 1\right)\mathbf{L_2} \otimes \mathbf{L_2} + \lambda_1 \lambda_2 \left(\mathbf{l_1} \cdot \mathbf{l_2}\right)\left(\mathbf{L_1} \otimes \mathbf{L_2} + \mathbf{L_2} \otimes \mathbf{L_1}\right)\right]. \tag{2-2}$$

where $\mathbf{l}_1 \cdot \mathbf{l}_2$ is a measure of the in-plane shear between the yarns. Also, define the two Lagrangian strains in, respectively, the $\mathbf{L}_1$ and $\mathbf{L}_2$ directions

$$E_1 = \frac{1}{2}\left(\lambda_1^2 - 1\right), \qquad E_2 = \frac{1}{2}\left(\lambda_2^2 - 1\right), \tag{2-3}$$

where $E_1 = \mathbf{L}_1 \cdot \mathbf{E}\mathbf{L}_1$ and $E_2 = \mathbf{L}_2 \cdot \mathbf{E}\mathbf{L}_2$ are the Lagrangian strains in the referential configuration. The referential balance of linear momentum is

$$\mathrm{Div}\mathbf{P} + J\mathbf{f} = \rho_0 \, \dot{\mathbf{v}} , \tag{2-4}$$

where $\mathbf{f}$ is the body force and lateral traction per deformed area, ρ_0 is the density in referential configuration, $\mathbf{P}$ is the first Piola-Kirchhoff stress tensor

$$\mathbf{P} = P_1 \mathbf{l}_1 \otimes \mathbf{L}_1 + P_2 \mathbf{l}_2 \otimes \mathbf{L}_2 \tag{2-5}$$

and J is the areal dilation defined by

$$J = \left[\det\left(\mathbf{F}^T \mathbf{F} \right) \right]^{1/2}. \tag{2-6}$$

It is intuitive that the magnitudes of the Piola-Kirchhoff stresses P_1 and P_2 in Eqn. (2-5) are related to the forces in the warp and fill yarns, respectively. Moreover, in-plane shear deformation is permitted, whereas the stresses are assumed to be independent of the shear deformation and are neglected. A constitutive law for the stress tensor $\mathbf{P}$ is derived by explicit consideration of the microstructure of the fabric.

2.2 Yarn scale

As shown in Figure 2-1 (b), the fabric is composed of interlacing yarns instead of a continuum membrane. Therefore the weaving yarns are considered to form the second scale level. In this scale, fabric structure characters are reflected and the yarn is considered as an elastica so that Bernoulli beam theory applies.

2.2.1 Governing equation of elastica

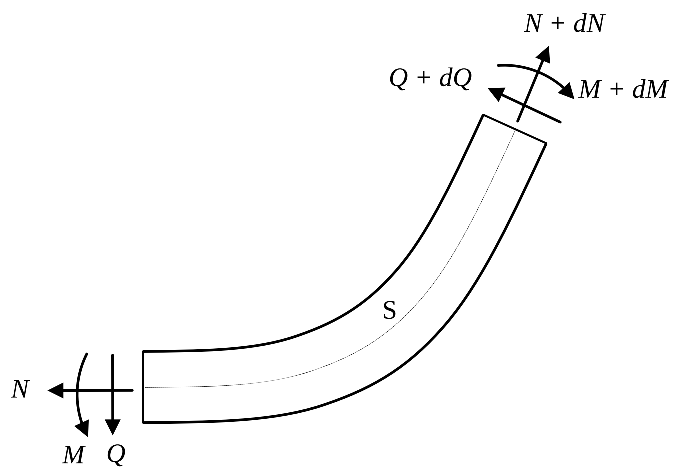

Figure 2-3 Description of the extensible elastica

As shown in Figure 2-3, a single yarn is modeled as an extensible elastica [27, 28]. When subjected to stretching and in-plane bending, the elastica deforms elastically. It is further assumed that the strain energy stored in the deformed configuration is

$$W = \frac{1}{2}B\gamma^2 + \frac{1}{2}A\delta^2 \tag{2-7}$$

where constitutive parameters B and A are the bending stiffness and the stretch stiffness of the elastica, respectively, and δ is the local elastica extension defined as

$$\delta = \frac{ds}{dS} - 1 . \tag{2-8}$$

γ is defined to reflect the bending strain of the elastica,

$$\gamma(S) = -\frac{d}{dS}\left(\phi(S) - \Phi(S)\right), \tag{2-9}$$

S and s are the length (location) parameter of the elastica in the reference and current configurations. The functions Φ and ϕ denote the yarn angles in the reference and deformed configurations (Figure 2-5), respectively. Thus, the bending moment M and internal axial tensile force N can be obtained,

$$M(S) = \frac{\partial W}{\partial \gamma(S)} = B\gamma(S) \quad \text{and} \quad N(S) = \frac{\partial W}{\partial \delta(S)} = A\delta(S) . \tag{2-10}$$

Also, the bending moment M and the internal shearing force Q is related as

$$Q(S) = \frac{dM(S)}{ds} = \frac{dM(S)}{dS}\frac{dS}{ds} . \tag{2-11}$$

Substitute Eqn.(2-10) into Eqn.(2-11), it becomes

$$\frac{d}{dS}\left(B\gamma(S)\right)\frac{dS}{ds} = Q(S) \ . \tag{2-12}$$

Since the bending stiffness *B* is not a function of the parameters *S* or *s*, Eqn.(2-12) can be rewritten as

$$B\frac{d}{dS}\gamma(S)\frac{dS}{ds} = Q \ . \tag{2-13}$$

By using Eqn. (2-9) and Eqn. (2-8), Eqn. (2-13) becomes

$$B\frac{d}{dS}\left[\frac{d}{dS}(\phi - \Phi)\right](1+\delta)^{-1} = -Q \ . \tag{2-14}$$

The internal tensile force $N(S)$, elastica extension $\delta(S)$ and stretch are related as

$$\delta(S) = \frac{N(S)}{A} \quad \text{and} \quad \mu(S) = 1 + \delta(S), \tag{2-15}$$

where μ is the local stretch of the elastica. Replacing the extension δ in Eqn.(2-14) with Eqn. (2-15), the governing equilibrium equation of the elastica is derived in terms of the bending stiffness *B* and stretching stiffness *A* as

$$B\frac{d}{dS}\left[\frac{d}{dS}(\phi-\Phi)\right]\left(1+\frac{N(S)}{A}\right)^{-1}=-Q\ , \tag{2-16}$$

which is a second order ordinary differential equation parameterized by the referential elastica length S.

2.2.2 Unit cell model of yarn weaving structure

As shown in Figure 2-1 (b), the fabric consists of two woven yarns. The single yarn is modeled as an extensible elastica subjected to stretching and in-plane bending. The index, *i* = 1, 2, is added to the equilibrium Eqn. (2-16) to indicate the two types of yarns,

$$B_i\frac{d}{dS}\left\{\frac{d}{dS}\left[\phi_i(S)-\Phi_i(S)\right]\right\}\left[1+\frac{N_i(S)}{A_i}\right]^{-1}=-Q_i(S) \quad \text{(no sum over } i\text{)}. \tag{2-17}$$

It is assumed that prior to the occurrence of damage, the stretching and bending stiffness are constants. But once damage is initiated the stiffness decreases with the degree of damage in the yarn. With presence of damage in a yarn, its stiffness is also assumed to be independent of the location *S*. Detailed constitutive relations between the stiffness and deformation of the yarn are formulated by an explicit consideration of the fibril scale and are discussed in following sections.

To mathematically model the behavior and coupling of the woven yarns, a unit cell model was introduced [14]. The unit cell contains two overlapping segments of the fill and warp yarns, each of them is of one-half of the yarn weaving period as shown in Figure 2-4 (description for one of the two yarns).

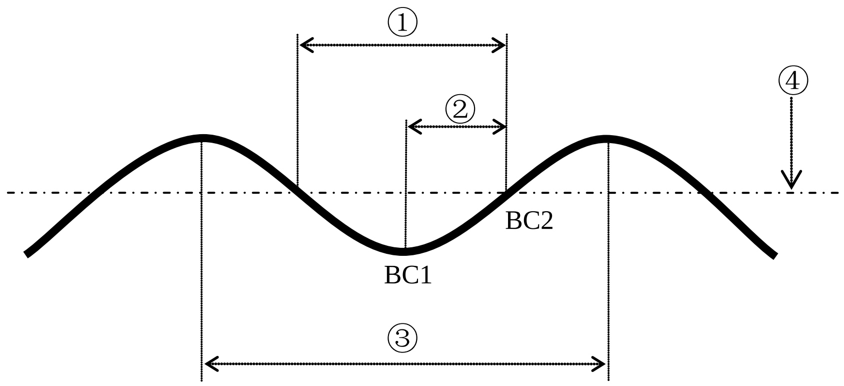

Figure 2-4 Description of the unit cell model

① Span of a unit cell, projected length is $2w_i$;

② Representative portion of the yarn used for the boundary value problem (described in Figure 2-5), projected length is w_i;

③ Span of a complete yarn weaving period;

④ Pseudo membrane surface (or projection surface).

The warp and fill yarns are assumed to deform symmetrically with respect to the midpoint (BC1) of the unit cell which is also the contact point of the yarns. Since the unit cell is assumed to deform symmetrically with respect to it midpoint, portion ② in Figure 2-4 is typical and sufficient to represent the boundary value problem.

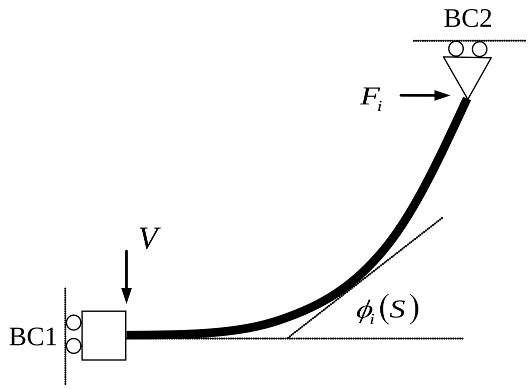

Figure 2-5 Boundary conditions of the unit cell model

Length of the this portion of yarn is L_{i}

The boundary and loading conditions on one half of each yarn segment is depicted in Figure 2-5, where F_i is the applied external force on the yarn by the neighbouring unit cell and V arises from the coupling between the overlapping yarns in the unit cell. The boundary conditions are

$$\text{BC1:} \quad \phi(0) = 0 \ , \qquad \text{BC2:} \quad \frac{d}{dS}[\phi(S) - \Phi(S)] = 0 \ , \qquad (2\text{-}18)$$

where BC1 is a statement of symmetry about the yarn's midpoint and BC2 is a moment free point since it is the intersection of the yarn with the membrane surface. The boundary conditions BC1 and BC2 constitute a mixed Neumann-Dirichlet boundary conditions problem. Next, the internal tension and shear forces are related to the external forces by

$$N_i(S) = F_i \cos\phi_i(S) + V \sin\phi_i(S), \tag{2-19}$$

$$Q_i(S) = V \cos\phi_i(S) - F_i \sin\phi_i(S), \tag{2-20}$$

The Lagrangian strain of the yarn is

$$\varepsilon_i(S) = \frac{1}{2}\left[\mu_i^{\,2}(S) - 1\right]. \tag{2-21}$$

The contact between the two overlapping yarns in the unit cell couples their deformation. This contact condition gives rise to a contact force V when the two yarns are in contact. The yarns are allowed to separate under certain loading conditions and in this case the contact force vanishes.

2.3 Fibril scale

A close-up observation indicates that the single yarn is composed of a large number of fibrils (Figure 2-1(c)), which may be misaligned with respect to the direction of the yarn. Because the fibril misalignment leads to non-simultaneous rupture of individual fibrils, the misalignment significantly affects the stiffness and failure pattern of the yarn in contrast to a yarn of perfectly-aligned fibrils. Even if a fibril deforms linearly up to sudden break [29], the yarn features a gradual and nonlinear process of rupture as qualitatively depicted in Figure 2-6.

The critical value in stretch marks the initial damage in the yarn, i.e. the first fibril breaks. This behavior is related to the damage in the yarn due to rupture of fibrils and is a constitutive property of the yarn.

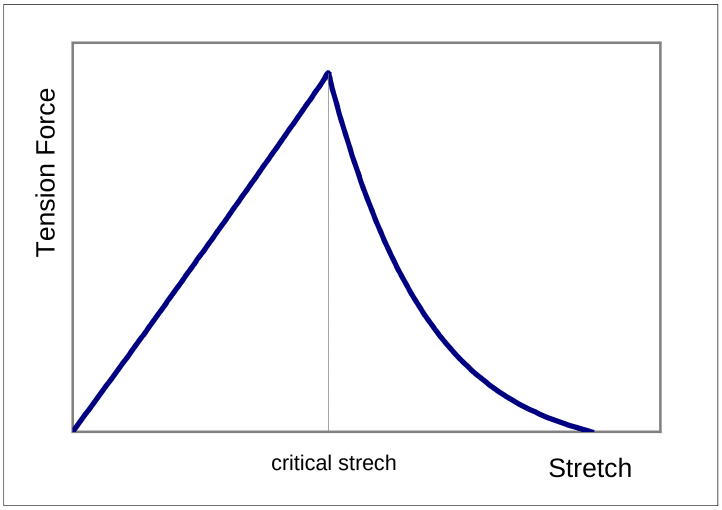

Figure 2-6 Qualitative description of the mechanical characters of a yarn

The importance of the fibril scale is that it tracks possible damage in the yarn through the rupture in individual fibrils, which is the realistic mechanism of the gradual damage in yarns.

Mathematical modeling of the deformation of the fibrils adopts the approach developed in [30] and [10], where the mechanical characteristics of yarns are described as the overall behavior of all the fibrils in a yarn through statistical computation. In the computation, the fibrils are randomly deployed within the width of a yarn (d_0 in Figure 2-7) and within a characteristic length of the yarn segment (h_0 in Figure 2-7).

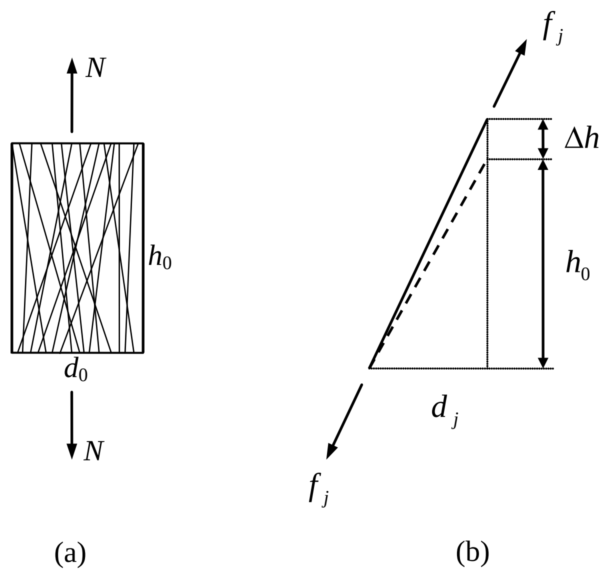

Figure 2-7 Description of fibrils

(a) fibril misalignment in a yarn segment;

(b) Deformation of one misaligned fibril

In Figure 2-7, d0 is the transverse dimension of a yarn, h_0 is determined by the spacing between the weaving yarns, N is the stretching force in the yarn, Δh is the extension along yarn direction and f_j is the tensile force in the j^{th} fibril. Each misaligned fibril is calculated for its particular stretch and tensile force. The stretching force N is equal to the summation of the projection of f_j in the yarn direction. As shown in Figure 2-7 (b), the stretch U_j of the j^{th} fibril is calculated by the geometrical relationship

$$U_j = \frac{\sqrt{(h_0 + \Delta h)^2 + (d_j)^2}}{\sqrt{(h_0)^2 + (d_j)^2}} \ , \qquad (2\text{-}22)$$

where $d_j = r_j d_0$ is a measure of misalignment of this fibril, and $0 \le r_j \le 1$ is generated randomly. As the overall response of n fibrils in a yarn, the effective modulus $E_I^{\ *}$ of the yarn is

$$E_I^{\ *} = \frac{E_I h_0^3}{n} \sum_{j=1}^{n} \frac{\rho_j}{\left(h_0^2 + d_j^2\right)^{3/2}}, \qquad \rho_j = \begin{cases} 1 & U_j < U_{crit} \\ 0 & U_j \ge U_{crit} \end{cases} \qquad (2\text{-}23)$$

where E_I is the elastic modulus of a fibril, and ρ_j tracks the rupture of a fibril and U_{crit} is the critical stretch of the fibril.

In order to measure and track the damage in the yarn, a damage parameter $\alpha \in [0,1]$ is defined as the fraction of non-ruptured fibrils. The damage parameter is determined by the largest yarn stretch experienced through the deformation history. The damage parameter is a monotonically non-increasing function of the stretch and it depends on the current and history stretch $\alpha(\mu, \mu^{hist})$. Furthermore, it is assumed that the dependence on the history is only through the maximum stretch $\mu^{h.\max}$ experienced by the yarn. Thus the damage takes the form

$$\alpha(\mu, \mu^{h.\max}) \ . \qquad (2\text{-}24)$$

In [10], the damage parameter α is derived based on the characteristic length (h_0 in Figure 2-7) of a yarn. It is assumed that the particular choice of the yarn's length does not affect the results. By employing the statistical approach presented above, the deformation behavior of a certain number fibrils is simulated. The number n of the fibrils is determined with reference to the fibril number of a physical yarn. The mechanical properties of a single fibril are published by Toyobo [29].

Based on the statistical approach, computation produces the stretching curve of the fibrils as their overall response. Through curve fitting, Eqn. (2-25) is obtained and is used to formulate the damage as a function of yarn stretch.

$$\alpha = \min\left(1, \quad \alpha^{hist}, \quad \frac{e^{-\beta\left(\mu^{\max} - \mu^{crit}\right)} - e^{-0.03\beta}}{1 - e^{-0.03\beta}} \right), \tag{2-25}$$

where β reflects the degree of fibril misalignment and is determined to be 124 through least square analysis [10], α^{hist} records yarn damages caused during their deformation history. The definition of the damage parameter makes it possible to track possible damages inside the yarn through monitoring the yarn stretch. Since the damage parameter is the fraction of non-ruptured fibril in the yarn, the stiffness of damaged yarn is assumed to be

$$A = \alpha A^0 \qquad \text{and} \qquad B = \alpha B^0, \tag{2-26}$$

where A^0 and B^0 are the initial (undamaged) stretching and bending stiffness of the yarn, respectively.

As one essential contribution of the fibril scale, the damage parameter is defined based on the statistical approach, which captures potential damage in the yarn and reflects the gradual damage process of the yarn. Determination of the stretching stiffness of the yarn, A^0, can be based either on experimental data or on the statistical approach. If the statistical approach is used, then the Young's modulus of the yarn (E_I^*) is computed as the effective Young's modulus of all the fibrils (Eqn.(2-23)). The stretching stiffness of the yarn can be obtained by combining the geometrical cross-section area and the second moment of the area of the undamaged yarn with the associated undamaged effective Young's modulus. Determination of the bending stiffness of the yarn, B^0, is complicated because it is affected by the friction between fibrils and therefore varies with changes in loadings. Details of bending stiffness determination are discussed in section 3.2. Once damage is initiated in the yarn, Eqn. (2-26) is used to update the stiffness of the yarn.

2.4 Coupling of the three scales

This section discusses coupling between the three scales to render a unified model of fabric materials.

First, the coupling between the fibril and yarn scale is established. Based on the statistical approach, the damage parameter, α_i, is defined to monitor the gradual damage in the yarn. The local properties A_i^0, B_i^0 of the yarns are obtained by a statistical or experimental study. The damage parameter is updated with the current stretch and stretch history and is used to evaluate the current stiffness of the yarn. Since the unit cell model consists of two overlapping yarns which may have different properties, the subscript $i = 1, 2$ is used to distinguish the warp and fill yarns. It should be noted that the two damage parameters α_i are functions of the deformation of the relevant yarn only. Thus, subscripts are added to Eqn.(2-24) which becomes

$$\alpha_i\left(\mu_i^{\max}, \mu_i^{h.\max}\right) \tag{2-27}$$

The current stiffness of the two yarns are

$$A_i = \alpha_i A_i^0 \quad \text{and} \quad B_i = \alpha_i B_i^0 \ . \tag{2-28}$$

The membrane scale and yarn scale are coupled by relating the extension in the membrane scale to the displacement in the yarn scale. The forces, F_i, in the yarn scale are then used to calculate the associate stresses in the membrane scale. For each yarn in the yarn scale, the projection on the tangent plane of the displacement of the end point BC1 relative to BC2 (Figure 2-4) is evaluated by

$$u_i = \int_0^{L_i} \left[\mu_i \cos\phi_i - \cos\Phi_i\right] dS \,, \tag{2-29}$$

where L_i is the length of the yarn portion ② (Figure 2-4). The same displacement measured in the membrane scale is

$$u_i = \left(\sqrt{1+2E_i} - 1\right) w_i \,, \tag{2-30}$$

where E_i is the membrane Lagrangian strain defined by Eqn. (2-3) and w_i is the half-length of the unit cell (Figure 2-4). Combining Eqns. (2-29) and (2-30) gives the kinematic coupling between the yarn and membrane scales. The membrane first Piola stresses, P_i, are related to the yarn external forces F_i by

$$P_1 = \frac{1}{2w_2} F_1 \,, \quad \text{and} \quad P_2 = \frac{1}{2w_1} F_2 \tag{2-31}$$

where $\frac{1}{2w_i}$ is the transverse yarn density in the reference configuration of the membrane. In other words, since the fabric is considered as continuum membrane in the continuum scale, the discontinuous external loads, F_i, that physically act on individual yarns are converted to distributed loads through Eqn. (2-31).

Chapter 3

Static Simulations[2]

3.1 Algorithm

Numerical solutions were obtained using one-dimension finite element method in conjunction with the Newton-Raphson method.

Starting with Eqn. (2-17), the yarn equilibrium equations were approximated through a Galerkin-based finite element method and were satisfied weakly using an element-wise integration. Coupling of the membrane scale and yarn scale was subjected to the geometric relations defined by Eqn. (2-29) and Eqn. (2-30). Integration of Eqn. (2-29) was approximated by Gauss quadrature. This procedure yields a system of nonlinear equations, including the constraint of non-negative yarn contact force V ($V = 0$ for separation and $V > 0$ for contact of yarns). The nonlinear system was solved through standard Newton-Raphson method with outputs of external forces F_i, maximum local stretches μ_i, angle ϕ_i of the yarns, and the contact force V. The forces F_i were then transmitted to the membrane

[2] A version of this chapter has been submitted for publication.

scale to find the first Piola stresses P_i in the membrane scale by Eqn. (2-31). The maximum local stretches μ_i are used to monitor the damage in the yarns through a secant-method procedure. Details of the numerical computation are referred to the Appendix.

3.2 Determination of the fabric properties

PBO Zylon AS fabric was chosen in the following static and dynamic simulations for the purpose of comparison with existing experimental data. Mechanical properties of the yarns at room temperature are listed in Table 1. Detailed mechanical properties and geometrical structure information of the Zylon fabric are available in the FAA test reports by Boeing Company [31] and by Arizona State University [32]. Basic properties of PBO Zylon material are referred to the technical document published by Toyobo Company [29]. Note that, as listed in Table 1, the current work distinguishes the warp and fill yarns in terms of the critical stretches, stiffness and degree of crimp.

For the current simulations, the stretch stiffness of yarns is obtained in the published documents [31]. Note that the stretch stiffness of the yarns may also be obtained through calculation based on Eqn. (3-1). The yarn stretch stiffness is the product of the effective Young's modulus and the cross-section area of the yarn (i.e. the summation of the cross-section areas of individual fibrils),

$$A^0 = E_I^* C \, , \tag{3-1}$$

where C is the cross-section area of the yarn and E_I^* is the yarn Young's modulus.

Table 1: Properties of 500 denier PBO Zylon yarn

Yarn type	Virgin yarn	Warp yarns	Fill yarns
Degree of crimp	0 %	3.1 %	0.6 %
Yarn length (L_i)		0.3741 mm	0.3650 mm
$\Phi_i(L_i)$		0.3481	0.1546
Yarn count (No./in.)		35 × 35	35 × 35
Stretch stiffness (N)	5114	4338	4724
Critical stretch	1.03	1.025	1.0297
Bending stiffness ($N{\cdot}mm^2$)	0.3095 Max 0.0619 Min	0.2657 Max 0.0531 Min	0.2935 Max 0.0587 Min
Cross-Section area	3.61×10^{-8} (m^2)		
Volume density	1560 kg/m^3		

There are difficulties in calculating the bending stiffness of the yarns even if the material has not been damaged. Theoretically, the bending stiffness of the yarn can be calculated as

$$B^0 = E_I^* I \, , \tag{3-2}$$

where I is the second moment of the cross-section area of the yarn. However, computation of the moment inertia incurs certain difficulties since the second moment of the cross-section area is not constant and keeps changing with loading conditions and the distribution of the fibrils within the yarn cross-section. Therefore, instead of using Eqn. (3-2), the bending stiffness is approximated by adopting Warren's method [33].

In addition to the linear density (deniers), yarn bending stiffness is primarily affected by the interaction between fibrils of the yarn. When loading is applied to the yarn, its fibrils are packed more tightly along each other, leading to stronger internal interaction and subsequently stronger bending resistance. Hence, the lower bound of the bending stiffness of the yarn is evaluated by assuming that the fibrils are loosely gathered and bend individually without interaction (friction). Thus the lower bound of the bending stiffness is the summation of the bending stiffness of all individual fibrils. If each fibril has a circular cross-section, then the yarn bending stiffness under zero or small loading conditions is

$$B_f = N \pi E_I r^4 / 4, \tag{3-3}$$

where r is the radius of a single fibril, N is the numbers of fibrils in the yarn and E_I is the Young's modulus of a fibril.

As for the upper bound, a simplified method is to treat the yarn as a solid rod of circular cross-section, then the bending stiffness is

$$B_s = \pi E_I R^4 / 4, \tag{3-4}$$

where R is the radius of the yarn's cross-section. However, a yarn is easily flattened under bending and significant reduction in its bending stiffness is expected. According to Warren [33], depending on the number of fibrils, the yarn bending stiffness is usually several times different between zero loading and sufficient loading situations. In the current work, the maximum bending stiffness is approximated to be five times the minimum.

As shown in Table 1, both the critical stretch and stiffness of the warp and fill yarns are reduced compared with the virgin yarn. This is because of the yarns are degraded during manufacturing process. The reduced critical stretch is not directly available in the published data, additional calculation is necessary to get the critical values based on the published data [31]. By applying the ultimate strength and corresponding stretch stiffness of the warp and fill yarns to Eqn. (2-15), the critical stretches of the warp and fill yarns were found to be $\mu_1^{crit} = 1.025$ and $\mu_2^{crit} = 1.0297$, respectively. Eqn. (2-15) relates the yarn stretch with the tension strength. The ultimate strength and the stretching stiffness of the fill and warp yarns are published in [31].

The referential shapes of the woven yarns [14] is approximated by the following function

$$\Phi_i(S) = \Phi_i(L_i)\sin(\pi S/2L_i), \tag{3-5}$$

where L_i are the half length of the yarn segments in the unit cell and $\Phi_i(L_i)$ are the yarn angles in the reference configurations at the boundaries BC2 (see Figure 2-4). Given the yarn crimp and $\Phi_i(L_i)$, the shapes of the woven yarns are uniquely determined by Eqn. (3-5).

3.3 Static Simulations

In this section, the static numerical simulations are implemented with various loading and boundary conditions. Throughout the following discussion, E_1 and E_2 are, respectively, the Lagrangian membrane strain along the warp and fill yarn directions.

3.3.1 Loading scenario No.1: uniaxial strain loading with $E_2 = 0$

Since the membrane strain is prescribed only in the warp direction, damage occurs merely in the warp yarns. The peak of the P_1 curve marks the initiation of damage in the warp yarns. In Figure 3-1 the damage in the warp yarns is indicated by the curve of the damage parameter α_1. Corresponding to the stress curve of P_1, the damage parameter α_1 is constantly equal to one prior to the peak, and decreases gradually untill zero after the initiation of damage. In comparison, the fill yarn also shows a similar rupture-like behavior with a similar loading peak. However, no damage is caused in the fill yarns as indicated by the damage parameter α_2 curve, which stays constant throughout the loading process. This behavior is due to the coupling of the fill and warp yarns in the yarn scale. Because of the damage in the warp yarns, their stiffness decreases gradually and, as a result, the contact force V decreases and leads to reduced force in the fill yarns.

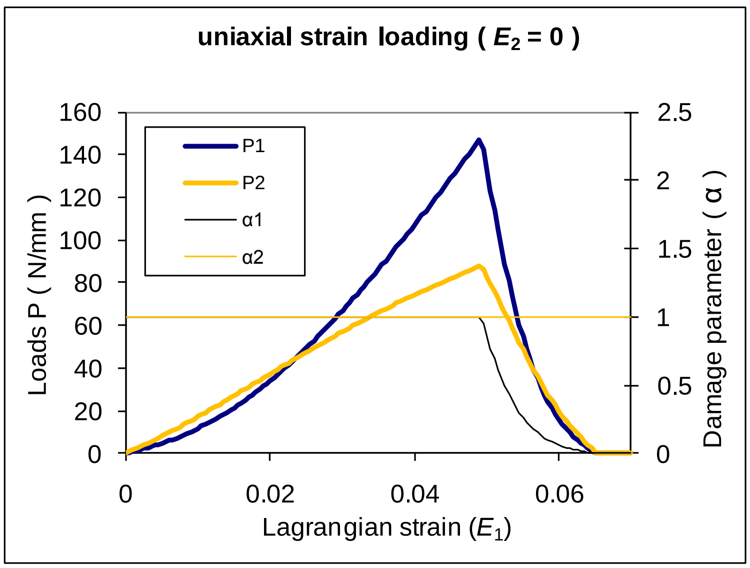

Figure 3-1. Loads P_1, P_2 vs. membrane strain E_1 with $E_2 = 0$,

E1 is monotonically increased up to complete damage in warp direction.

Moreover, in contrast to the critical strain ($\varepsilon_1^{crit} = 0.0253$) of the warp yarn, the fabric's critical strain is approximately at $E_1^{crit} = 0.049$ and the yarn's failure is complete at approximately $E_1 = 0.066$. This large difference is explained by the crimp of yarns in the weaving structure, which increases the sustainable deformation capability of the fabric compared to the underlying yarn.

3.3.2 Loading scenario No.2: loading, unloading and reloading process

In order to further visualize the damage evolution in the yarns, the current deforming scenario incorporated an unloading-and-reloading process during a stage of partial failure in the yarns. Similarly, as in loading scenario No.1, the strain E_1 was controlled while keeping $E_2 = 0$. Shown in Figure 3-2, the thick-line paths denote the initial loading process, and thin-line paths denote the unloading and reloading process.

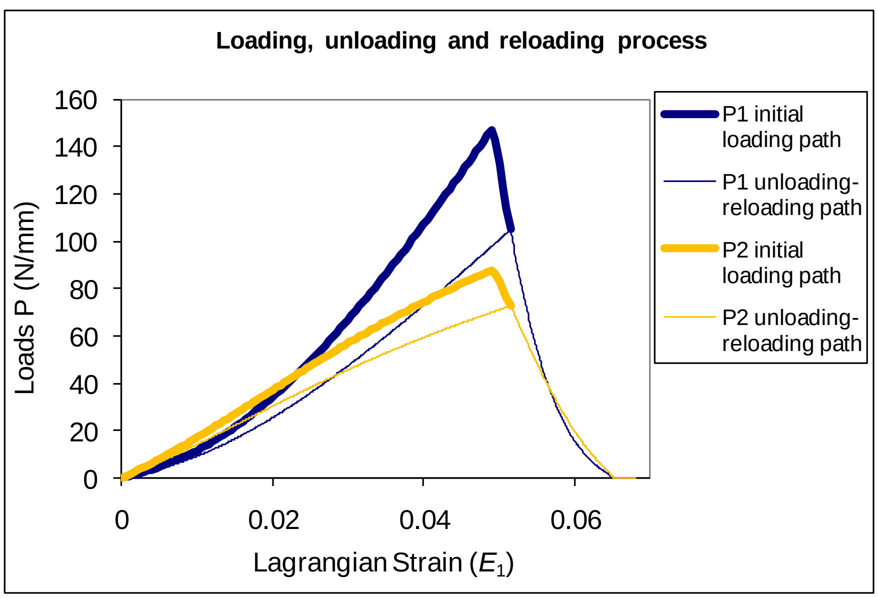

Figure 3-2. Loads P_1, P_2 vs. E_1 with $E_2 = 0$,
E_1 is loaded, unloaded at partial damage stage
and reloaded till complete failure.

Naturally, the unloading-reloading paths deviate from the initial loading paths in that the damage has already been caused during the initial loading process. Once the reloading reaches the same strain level as in the initial loading process, the reloading paths continue exactly with the original courses. In this case no residual strains are present when the load is removed. This is a direct result of the weaving property that the coupling force V vanishes whenever the forces F_1 and F_2 vanish.

3.3.3 Loading scenario No.3: equal-bilateral stretching

Under equi-biaxial stretching ($E_1 = E_2$), the fabric shows another interesting behavior. As shown in Figure 3-3, the stress curve P_1 features two peaks in the process, while stress curve P_2 features only one. With reference to the damage parameter curves α_1 and α_2, it is found that the damage in the warp yarns is initiated at the second peak. The first peak in the P_1 curve is actually caused by the initiation of damage in the fill yarns. This explains the simultaneous occurrence of the first peaks of P_1 and the only peak of P_2. Under the current loading condition, due to lower degree of crimp in fill yarns, the damage in the fill yarns is initiated, approximately at $E_1 = 0.029$, much earlier than in the warp yarns and grows to complete failure rapidly at $E_1 = 0.0325$. Compared with loading scenario No.1, damage in warp yarn is delayed and the strain at complete failure reaches $E_1 = 0.091$, well above the value in loading scenario NO.1.

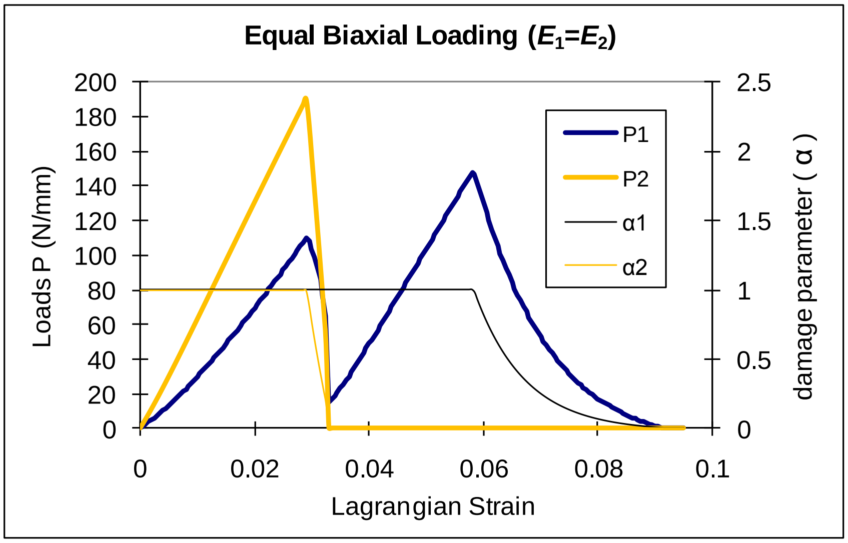

Figure 3-3. Equally biaxial loading $E_1 = E_2$

till complete failure of both yarns.

The explanations for this behavior can be found in the weaving structure of the fabric. Due to the lower degree of crimp in fill yarns, under the circumstance of equi-biaxial stretching conditions, the fill yarns were straightened up much faster than the warp yarns. In contrast to loading scenario No.1, once the fill yarns completely failed the contact force vanishes. Without constraint from the interaction of fill yarns, the warp yarns can be completely straightened up and, macroscopically, show increased deformation capacity.

3.3.4 Loading scenario No. 4: uniaxial stretching with $P_2 = 0$

The loading in this case is uniaxial tension along the warp yarns while keeping the fill yarns unconstrained ($P_2 = 0$). Comparison with experimental data is presented in Figure 3-4. Note that the Lagrangian strain is used in Figure 3-4 instead of the engineering strain used in the experiment [31], in which a uniaxial tensile test was applied on a strip of Zylon fabric along the warp yarns (yarn count 35×35, 1.5 inches wide and 4 inches gage length). The current simulation shows excellent agreement with the experimental results as shown in Figure 3-4.

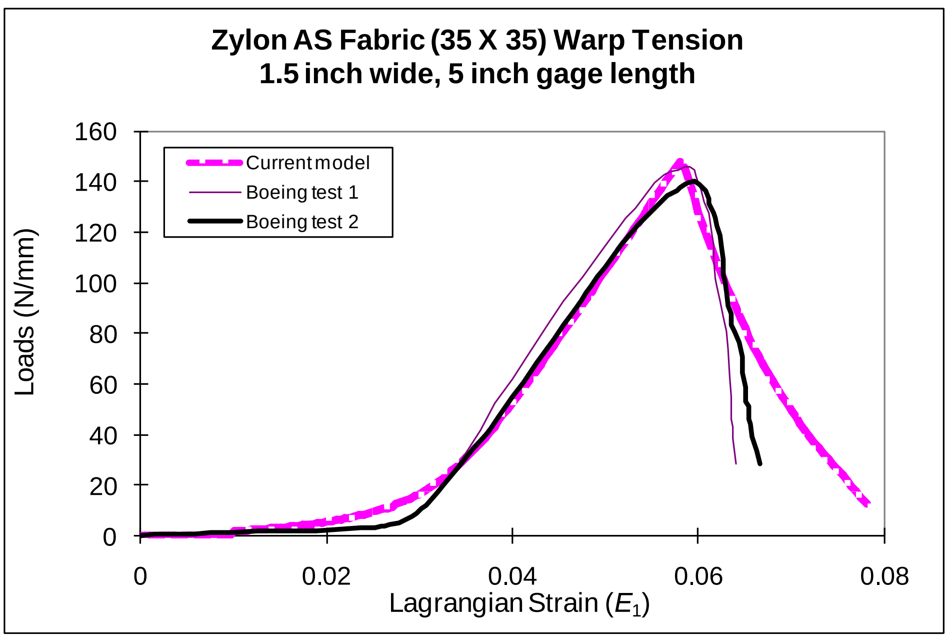

Figure 3-4 Uniaxial tension in warp direction with $P_2 = 0$

Additional demonstration of the weaving structure is shown in Figure 3-5, where the dependence of E_2 on E_1 under uniaxial loading is shown.

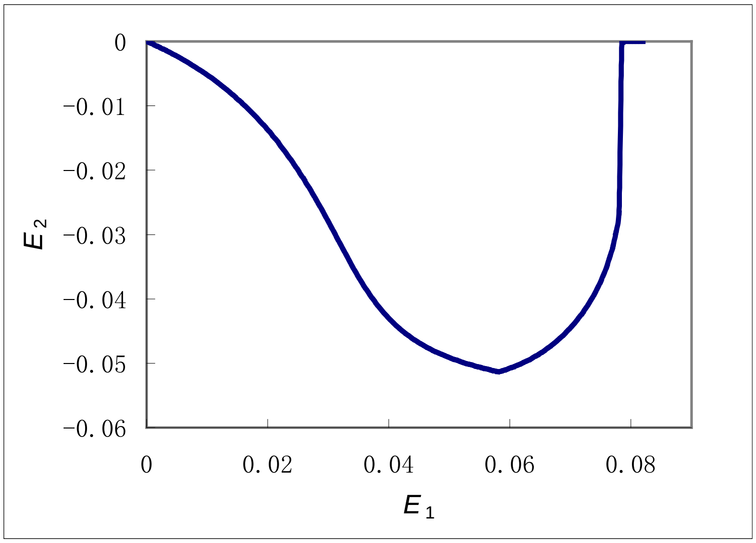

Figure 3-5 E_1 vs. E_2 with $P_2 = 0$

This dependence is a Poisson-like effect induced by the weaving structure and yarn interaction. Since the fabric is free of constraint in the fill direction (E_2), it shrinks transversely while stretched in the warp direction. Once damage is initiated in the warp yarns, the coupling between the two yarns diminishes gradually and the fill yarns stop shrinking and start expanding back to their initial shape.

3.3.5 Effect of bending stiffness

As discussed in section 3.2, the yarn bending stiffness is not constant even before damage because it is affected by the loading conditions of yarn. To investigate the influence of the bending stiffness, the uniaxial loading simulation is repeated with the upper and lower limits of the bending stiffness in the fill yarns (B_2) as shown in Figure 3-6.

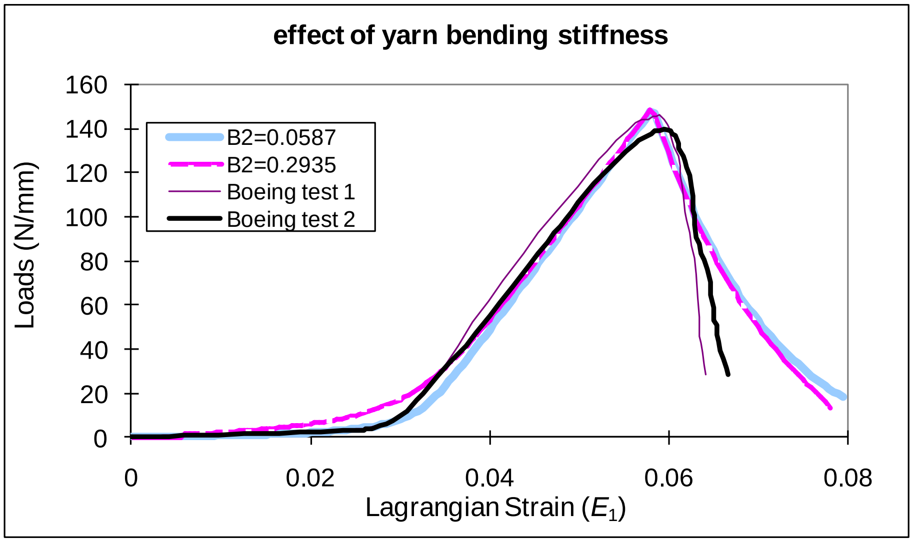

Figure 3-6 Uniaxial tension in warp direction with $P_2 = 0$ for the demonstration of bending stiffness

Comparison with experimental results demonstrates that during the early stage of loading the bending stiffness dominates the load-deflection behavior of the fabric. Since the fill yarn is unloaded ($P_2 = 0$), the simulation with lower bound of B_2 indicates a better agreement with the experiment. With load increasing, effect of bending stiffness on the fabric behavior becomes negligible.

3.3.6 Summary

The static simulations verify the expected abilities of the current material model. It reflects the interaction between yarns as demonstrated through various phenomena under different loading and boundary conditions. The gradual damage of fabric is nicely captured. At the early stage of the fabric deformation, the fabric behavior is mainly determined by the yarn bending stiffness and the degree of yarn crimp.

Chapter 4

Dynamic Simulations[3]

In this chapter, dynamic simulations are implemented for PBO Zylon AS fabric to study the ballistic behavior of the fabric. The same material properties are used as in static simulations (Table 1). The finite element simulation package ABAQUS 6.9 was used for the dynamic simulations.

4.1 FEA Model Setup

In order to verify the material model, the FEA simulation model in ABAQUS (Figure 4-1) is created with reference to the experimental work of the ballistic impact on fabric by Verzemnieks in Boeing Company [31]. In the experiment, the projectile is a flat-ended cylindrical steel projectile of 37.1g, the fabric is a square-shaped PBO Zylon (10.75”×10.75”). The fabric is gripped at its two edges and is impacted at its center by the projectile with various initial velocities. The simulation model follows the same settings as in the experimental work, including the boundary conditions, shape, size and mass of the projectile and the fabric.

[3] A version of this chapter has been submitted for publication.

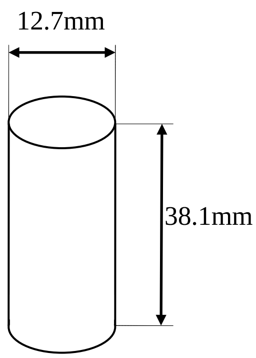

(a) Cylindrical projectile (mass = 37.1g)

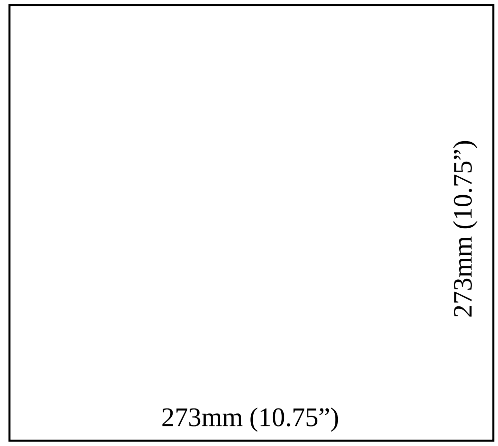

(b) Fabric (thickness = 0.05 mm)

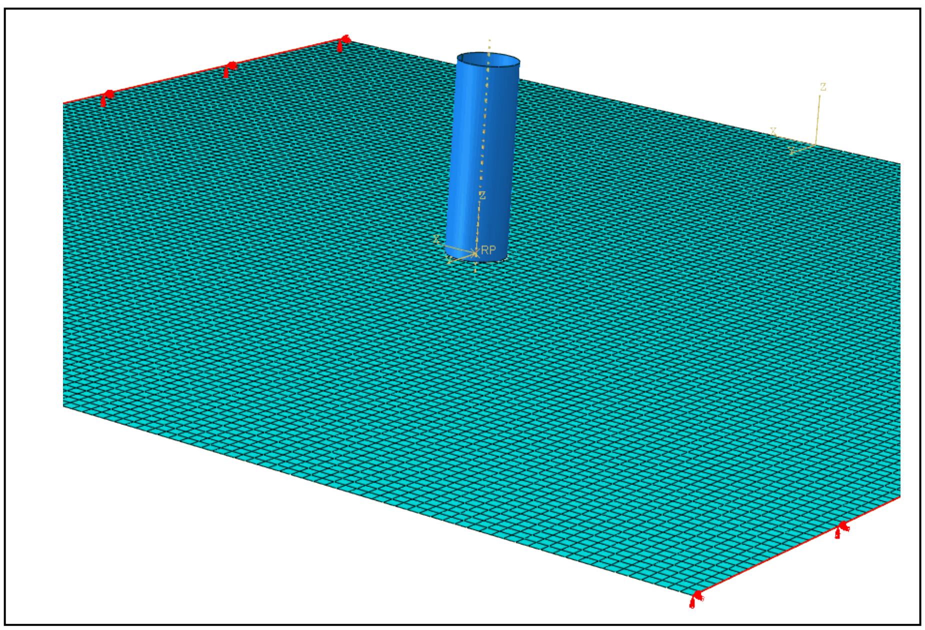

(c) Model assembly

Figure 4-1 FEA model illustration

With reference to Rebouillat’s investigation [34], the friction between the steel projectile and the Zylon fabric is approximated as 0.5 for the current simulations. As indicated in [34], the kinetic friction properties on Kevlar fabric are dependent on the interfacing material and the relative sliding speed. The friction is 0.27 between Kevlar fibers and 0.55 between fibers and metals. A friction coefficient of 0.5 was chosen for the current simulations based on the assumption that Kevlar fabric and Zylon fabric have the similar frictional properties.

The thickness of the fabric is not involved in the current material model, but it is required in ABAQUS when the fabric is modeled in membrane elements. The thickness of the membrane is calculated by equating the volume or the mass of the realistic fabric material and the membrane model. The thickness is maintained constant during simulations and the Poisson ratio is thus set to zero. Since the damage in the fabric is controlled by yarn stretch and both the yarn stretch and the resistance on the projectile are related to the in-plane resistance forces in the fabric, so the thickness of the membrane is not crucial as long as the user-defined nominal stress matches the thickness. But the membrane thickness can not be a very large value and should be comparable with the realistic dimension in order to avoid contact issues in ABAQUS.

In this work, the user-defined material is coded in Fortran and is implemented with ABAQUS Explicit subroutine VFABRIC. The subroutine provides the nominal strain in the fabric and asks for nominal stress from the user. Detailed instructions can be referred to ABAQUS User Subroutine Reference Manual section 1.2.3. The projectile is modeled as an analytical rigid body and kinematic formulation is chosen for the contact algorithm between the projectile and the fabric.

Due to the anisotropy nature of the fabric, definition of material orientation is necessary. Definition of the material orientation involves two steps. The first step is to define the local coordinate system attached to the fabric. The second step is to define the yarn directions in the referential configuration. The yarn directions are not necessarily orthogonal in undeformed fabric. If the yarn directions are not explicitly defined, ABAQUS assumes that the yarns are initially aligned with the local coordinate system. ABAQUS tracks the local deformation and automatically updates the local coordinate systems. The local coordination system is maintained as an orthogonal system, but the yarns may be rotated. The yarn directions in the deformed configuration are determined through the shear strain in the membrane. More detailed information is referred to ABAQUS Analysis User's Manual section 19.4.1.

Since the fabric is modeled with membrane elements, all tensor output variables are stored with reference to the local coordinate system (ABAQUS Analysis User's Manual section 4.2.1). The local coordinate system rotates with the average rigid body spin of the fabric material. The storage of these tensor output variables at each material calculation point is updated corresponding to the rotation of the local coordinate system (ABAQUS Theory Manual section 1.5.4).

In the subroutine, the damage status in the fabric is stored in three variables, SDV1, SDV2 and SDV3. Two variables are evaluated with the damage parameters, SDV2 = α_1, SDV3 = α_2. DV1 is evaluated as 1 or 0 and is used as a damage flag for the purpose of element deletion. DV1 = 0 only if both α_1 and α_2 are equal to zero, which indicates complete failure in both warp and fill yarns. Table 2 describes these legend symbols.

Table 2: Explanation of damage state symbols

Legend symbol	Description
SDV1	SDV1 = 0 when both SDV3 = 0 and SDV2 = 0, otherwise SDV1 = 1.
SDV2	SDV2 = α_1, the state variable monitoring the damage status of the fabric in warp yarns.
SDV3	SDV3 = α_2, the state variable monitoring the damage status of the fabric in fill yarns.

In the simulations, a well defined FEA model requires the definition of both the material orientation and the boundary condition. To simplify the description of boundary conditions and material orientation directions, the following notation conventions are created. The part assembly and fabric boundary conditions are referred to the global X-Y-Z coordination system, and the material orientation is referred to the local *x*-*y*-*z* coordinate system. For the current simulations, the *x* direction always indicates the warp yarns and *y* direction for the fill yarns. Z and *z* directions are always the same in the referential configuration but not in the deformed configuration. With the help of Figure 4-2 and Table 3, the naming convention for yarn orientation and fabric boundary conditions is introduced.

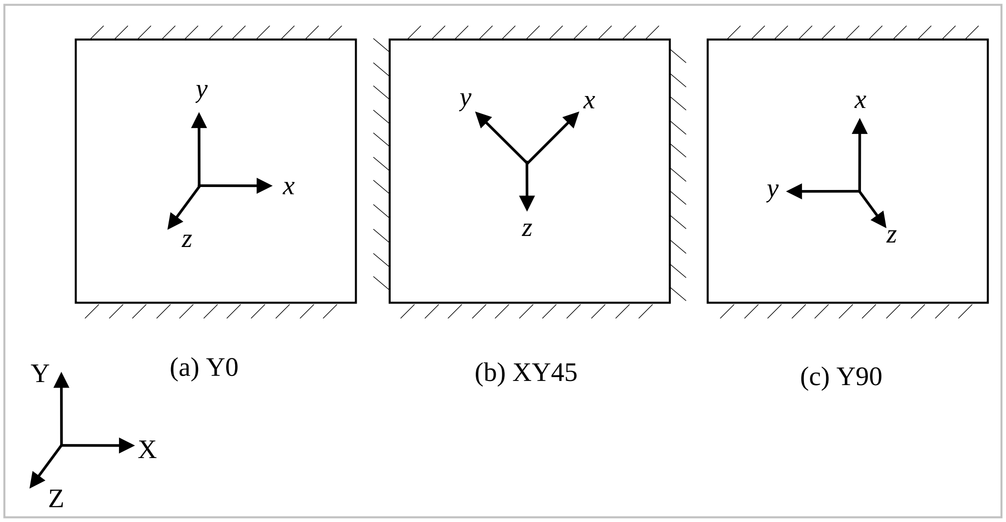

Figure 4-2 Notation definition for
fabric orientation and boundary conditions

Table 3: Naming convention for material orientation and boundary conditions

Notation names	Description
X-Y-Z	the global coordinate system, referred by (1) FEA model assembly (2) fabric boundary conditions
x-y-z	the local coordinate system of the fabric, defining the material orientation
Y0	two-edge fixed in Y direction and material orientated at 0°
XY45	four-edge fixed and material rotated by 45°
Y90	two-edge fixed in Y direction and material rotated by 90°

As shown in Figure 4-2, (a) Y0 means the two normal-to-Y edges are fixed and the material orientation coordinate system is aligned with the global system, i.e. the fill yarns (*y* direction) are fixed and warp yarns (*x* direction) are free of constraints at the fabric boundaries. (b) XY45 means the fabric are fixed at all its four edges and the material orientation is rotated 45°, i.e. the warp and fill yarns form a 45° angle relative to the edges (c) Y90 means the material is rotated 90°, i.e. the warp yarn is fixed at fabric boundaries while the fill yarns free of constraints.

4.2 Comparison with experimental results

For the purpose to compare with the experimental work, in this section the fabric is applied Y90 conditions. The fabric is two-edge-fixed in the warp yarn direction.

Figure 4-3 and Figure 4-4 show the velocity curves of the projectile, and the projectile either is rebounded or penetrates the fabric. In the figures, the projectile velocity changes much slower at the early stage of impact. This is accounted by the crimp of yarns and the initial deformation is dominated by yarn decrimping that results in very little resistance force on the projectile. Once the yarns are straightened, the resistance increases sharply until the projectile is rebounded (Figure 4-3) or penetrates the fabric (Figure 4-4).

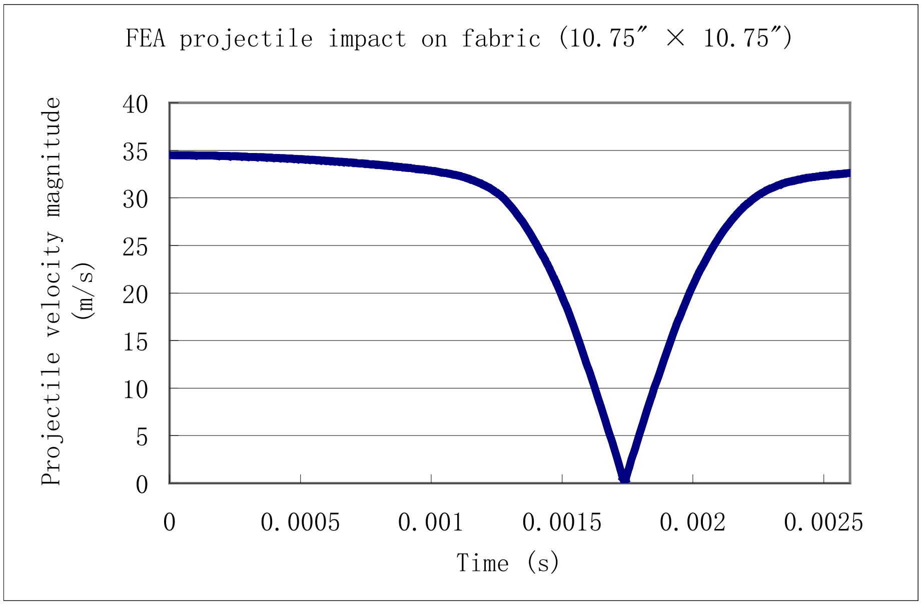

Figure 4-3 Projectile is bounced back with V_0 = 34.5m/s (Y90)

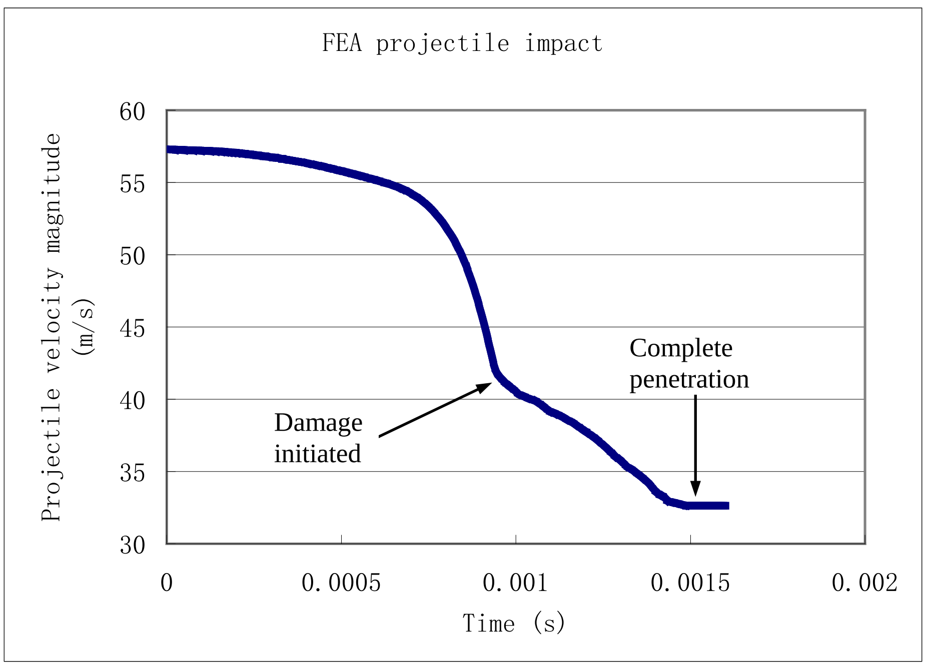

Figure 4-4 fabric perforated with V_0 = 57.3m/s (Y90)

Figure 4-5 shows the stress change in time of an element at the center of the fabric. Because of the crimp of yarns, the stress initially changes slowly and then increases sharply during later stage of the impact up to complete damage in the fabric. Slight vibration in the stress curve is noticed, this is caused by the longitude stress wave and the transverse swaying of the fabric during the impact.

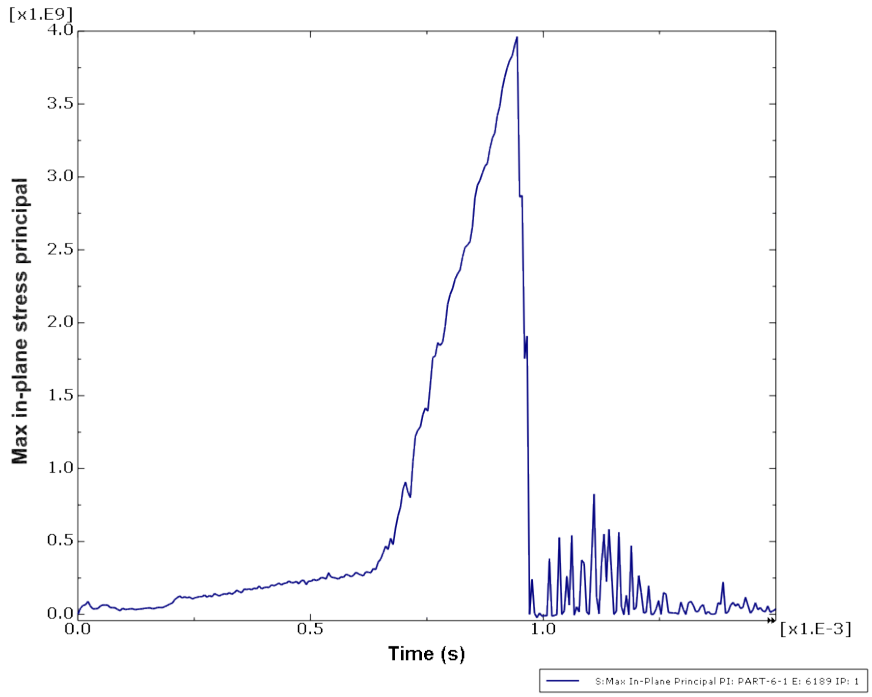

Figure 4-5 Stress (N/m^2) change in time at the center of the fabric

V_0 = 57.3m/s (Y90)

The stress curve in Figure 4-5 takes on a quite similar appearance in comparison with Figure 3-4. In fact, since the current model does not incorporate dynamic material properties, the stress curves should look similar under the same boundary condition. However, unlike Figure 3-2 and Figure 3-4, the fabric appears to break in a sudden manner as shown in Figure 4-5. This because the simulation data was sampled using a long time interval such that more detailed information during the rupturing process was not recorded.

In Table 4, the simulation results are compared with experimental data [31]. According to the experiment, the projectile is bounced back when the initial impact velocity is 34.5m/s. With other higher impact velocities listed in the table, the fabric is penetrated and thus the critical velocity should be a value between 34.5 m/s and 39.78 m/s.

Table 4: Comparison between simulations and experimental data

Initial impact velocity (m/s)		34.5	39.78	57.3	83.06	123.69
Residual velocity (m/s)	Simulations	Bounced back	10	32.6	66.83	110
	Experiment	Bounced back	5.67	29.99	61.54	97.99
Projectile energy loss (%)	Simulations	100%	93.7%	67.6%	35.3%	20.9%
	Experiment	100%	97.97%	72.6%	45.1%	37.23%
Absorbed energy (J)	Simulations	21.69	27.5	41.18	45.13	59.3
	Experiment	21.69	28.75	44.22	57.88	105.66
Max normal deflection (mm)		50.91	51.85	51.75	51.13	51.25

According to the comparison listed in the table above, the simulation results show agreement with the experimental data. In the simulations, the projectile is rebounded when V_0 = 34.5 m/s and the fabric is penetrated with higher impact velocities. It is noted that the residual velocities from simulations are always greater than the experimental data. It is pointed out in the experiment report [31] that the fixed edges of the fabric slipped a short distance during the impact, which accounts for a portion of the energy absorption in the experiment. However, this portion of energy is not accounted by the simulations. Also, inter-yarn friction and the air impedance on fabric deflection are not considered in the simulations.

One weakness of the current model is the inability of modeling inter-yarn friction. As far as the fabric static behavior is concerned, the importance of the yarn-to-yarn friction is negligible. This is supported by the comparison between the static numerical simulations and experimental results. As shown in the static numerical simulations (Section 3.3), the results agree considerably well with the experimental work. However, during dynamic impact, the inter-yarn friction involves more material resistance and leads to higher energy absorption. It is believed that the interactional friction between woven yarns play an important role in accounting for the dynamic behavior of the fabric. Therefore, the ignorance of inter-yarn friction is attributed to underestimation of absorbed energy in the dynamic simulations.

4.3 Damage mechanism

Various damage manners can be observed in the simulation with changes in impact conditions. In this section, damage modes are introduced along with demonstration of more simulation results.

4.3.1 Local damage

Local damage means the material failure occurs at the direct impact area and/or immediate neighbourhood.

Figure 4-6 shows the local damage pattern obtained from the FEA simulations with two-edge fixed boundary condition (Y90) and an initial projectile velocity of 57.3m/s. As shown, local damage occurs in both warp and fill yarns at the direct impact area. Some elements are completely damaged and some are partially damaged. By comparing Figure 4-6(a), (b) and (c), the elements that are damaged in both directions or in only one direction can be identified. The completely damaged elements form a similar-looking hole as observed in the experiment [31]. The highly localized damage in the experiment [31] is believed to occur because of the sharp edge of the flat-end cylindrical projectile by Zohdi et al. [10].

As annotated in Figure 4-6 (c), the partial damage for this particular simulation is due to damage in warp yarns only. This type of partial damage is also observed in experiment [31] except that the partial damage in experiment results from yarn pull-out mechanism. In the simulation, the yarn relative slip is not allowed, so the simulated partial damage is due to complete damage in merely one direction.

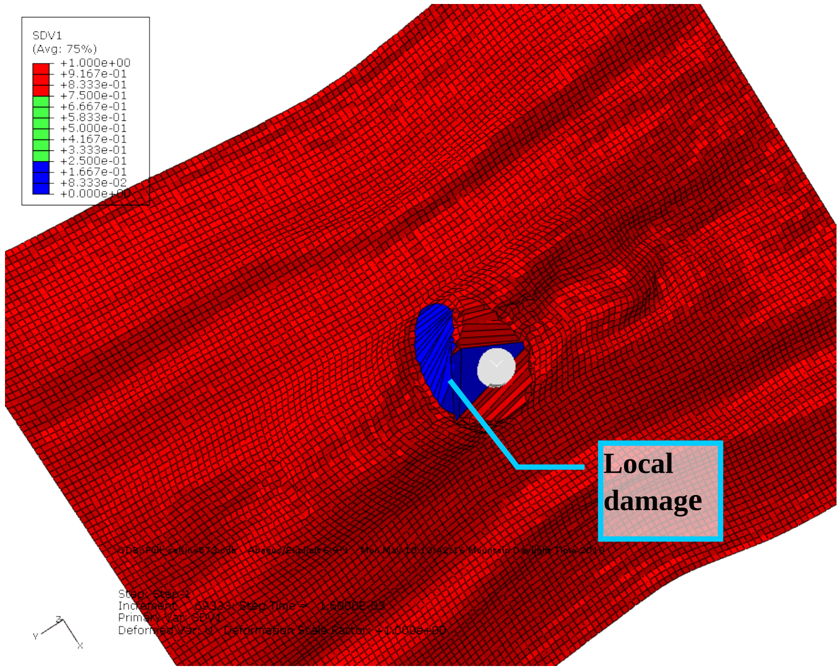
SDV1
(Avg: 75%)
+1.000e+00
+9.167e-01
+8.333e-01
+7.500e-01
+6.667e-01
+5.833e-01
+5.000e-01
+4.167e-01
+3.333e-01
+2.500e-01
+1.667e-01
+8.333e-02
+0.000e+00
Local damage

(a) SDV1

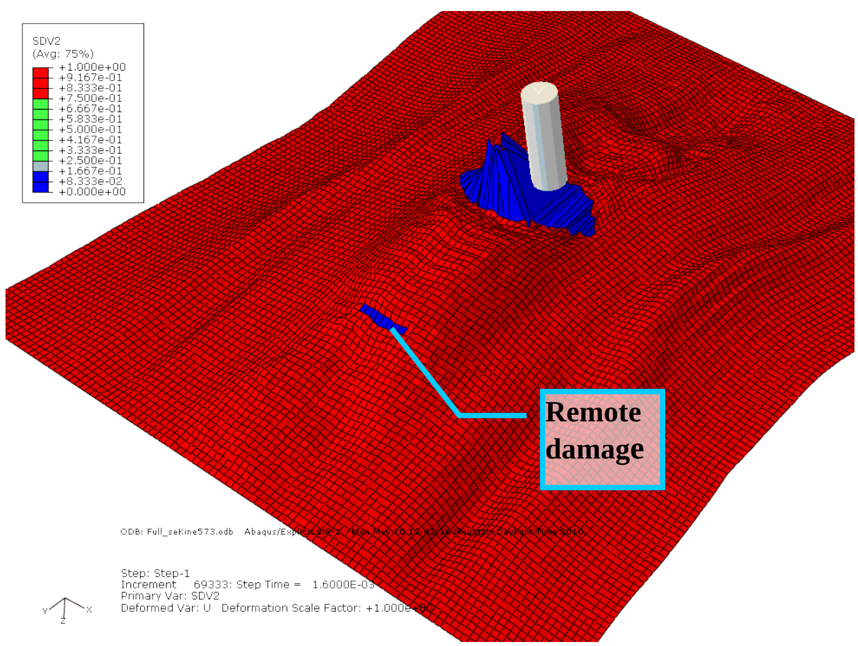
SDV2
(Avg: 75%)
+1.000e+00
+9.167e-01
+8.333e-01
+7.500e-01
+6.667e-01
+5.833e-01
+5.000e-01
+4.167e-01
+3.333e-01
+2.500e-01
+1.667e-01
+8.333e-02
+0.000e+00
Remote damage
Step: Step-1
Primary Var: SDV2

(b) SDV2

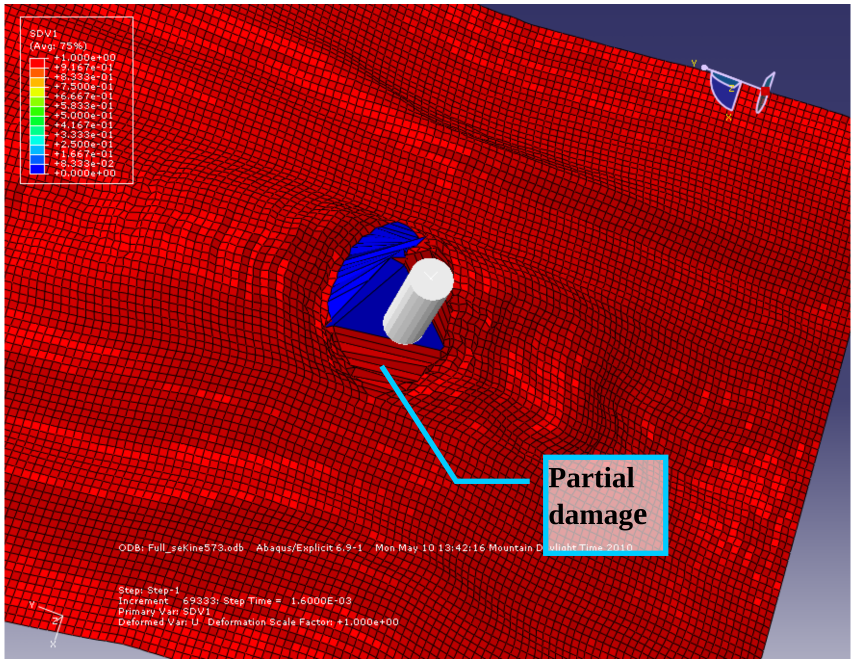

(c) SDV3

Figure 4-6 Local damage pattern (Y90)
friction coefficient = 0.5 and V_0 = 57.3 m/s

Slight difference in the damage patterns is also noticed between the simulations and the experiment. As highlighted in Figure 4-6(b), in addition to similar penetration damage at the impact neighbourhood, minor remote damage is noted away from the direct impact area.

4.3.2 Remote damage

Remote damage occurs at sites away from the direct impact area, as shown in Figure 4-6 (b). It could happen anywhere between the directly impacted site and the fixed boundaries. The following simulation (Figure 4-7) shows more apparent and severe remote damage. Experiment observation of this type of damage can be found in [24], where both local damage and severe remote damage are observed. Moreover, another failure mode, namely yarn pull-out failure, is also observed in [24].

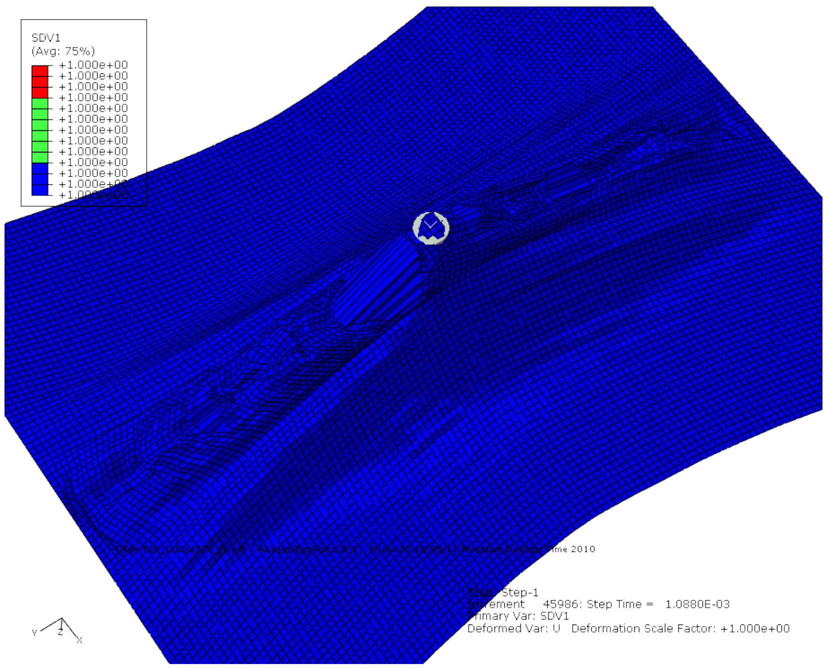

(a) SDV1

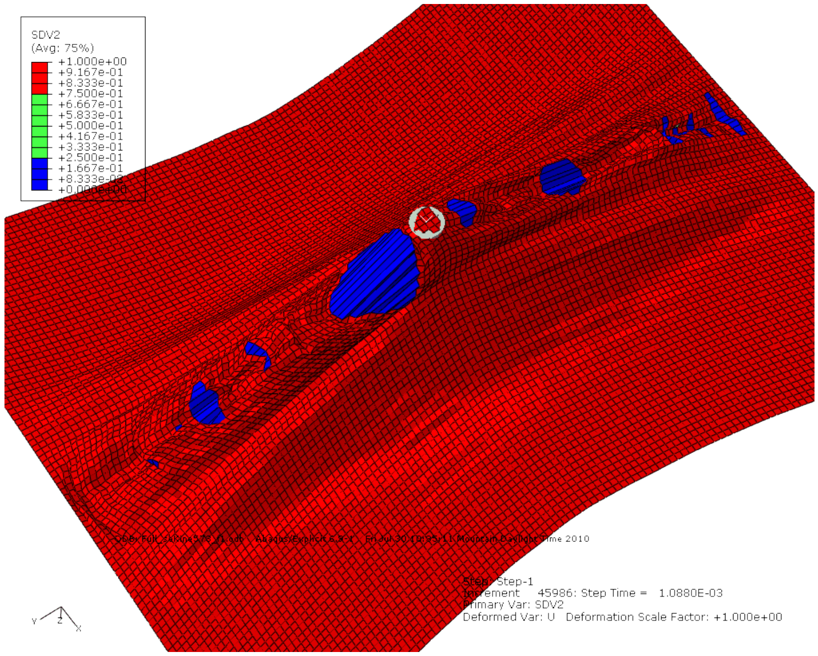

(b) SDV2

Figure 4-7 Remote damage pattern (Y90)

friction coefficient = 0.1 and V_0 = 57.3 m/s

This dynamic simulation is compared with the quasi-static push test experiment in [24]. There are two arguments for this comparison. First, the dynamic properties are not involved in the current material model. Second, a low level of friction is applied in this simulation. Therefore, similarity in material behavior can be expected between the simulation and the quasi-static push test.

4.3.3 Yarn pull-out failure

Yarn pull-out failure is observed in experiment [24]. This type of failure is due to the relative sliding between inter-woven yarns. Whereas the current material model is not able to simulate such phenomenon. This is because the constraining boundary condition (as defined in Figure 2-5) is imposed on the current material model and relative sliding between yarns is not allowed.

4.4 Influence factors on damage mechanism and energy absorption

The ability to absorb impact energy is the essential criterion for assessment of the fabric ballistic performance. Investigation reveals there are a number of factors that can affect the damage patterns and/or energy absorption. These factors are discussed in the following sections and they may not be a complete list of all possible influence factors.

4.4.1 Projectile-fabric friction

The influence of the friction between the projectile and the fabric depends on the friction coefficients. Based on the simulations, if the friction lies in a certain range, the simulation results of damage modes and energy absorption are not sensitive to changes in the friction coefficients. As an example, comparing Figure 4-6 (friction = 0.5) with Figure 4-8 (friction = 2.0), similar results are obtained.

However, the projectile-fabric friction helps maintain the contact between them and prevent relative slipping, such that the projectile-fabric friction holds the yarns to move along with the projectile. To investigate the influence of the friction, the simulation results are compared between Figure 4-7 (friction = 0.1) and Figure 4-8 (friction = 2.0), where the only difference lies in the friction coefficients. It is noticed that friction level does significantly affect the manner of damage. At low friction level, remote damage tends to occur. On the contrary, high friction level tends to cause more localized damage. It is because high level friction induces stress concentrations around the contact area and thus tends to cause local damage.

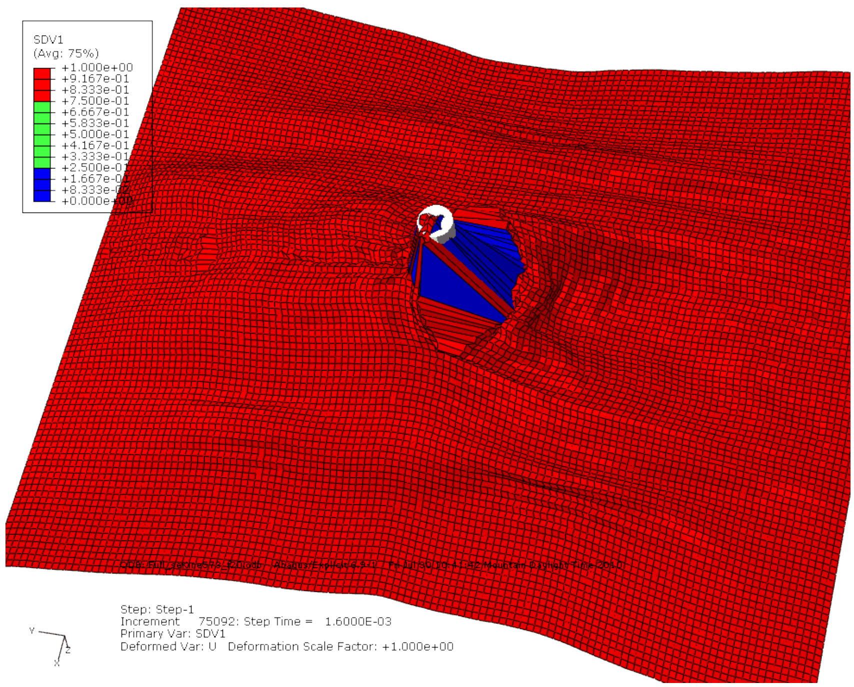

(a) SDV1

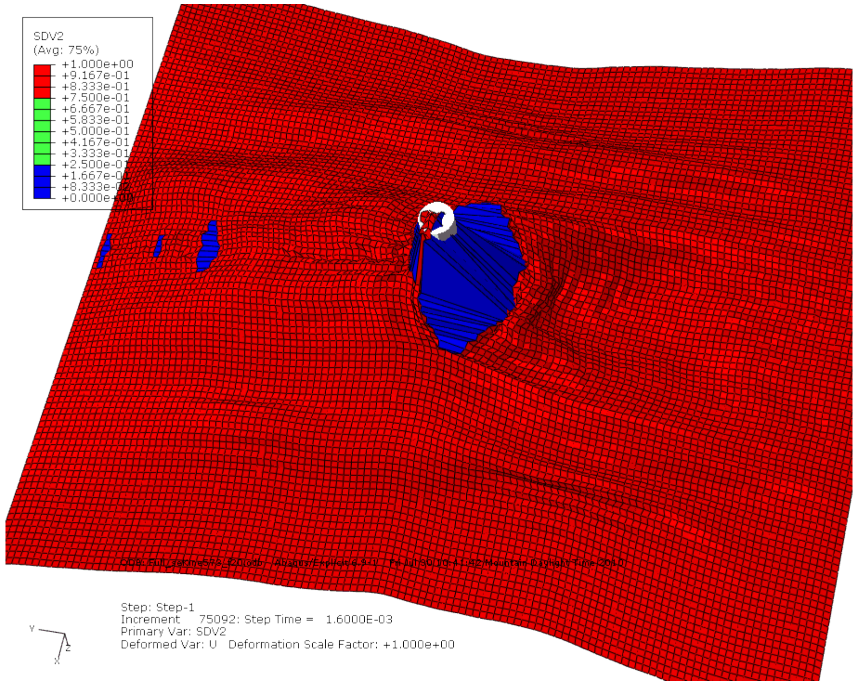

(b) SDV2

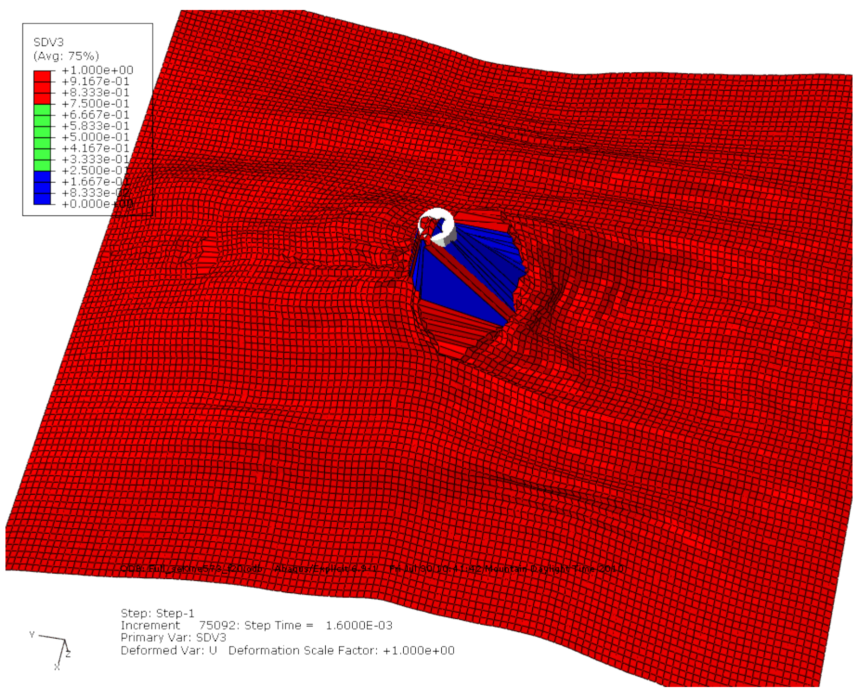

(c) SDV3

Figure 4-8 Influence of projectile-fabric friction (Y90)

Friction coefficient = 2.0 and V_0 = 57.3 m/s

4.4.2 Boundary conditions

Boundary conditions significantly affect the impact response of the fabric. To demonstrate and compare the effect of different boundary conditions, two kinds of boundary conditions, Y90 and XY0, were applied to the fabric.

The simulations show that, when the fabric is four-edge fixed, the damage is usually highly localized at the direct impact contact. If the two-edge fixed boundary condition is applied, remote yarn failure can be observed. The simulations shown in Figure 4-6 and Figure 4-9 are different in the boundary conditions. When two edges are fixed, remote damage occurs (Figure 4-6(a)). In contrast, Figure 4-9 shows highly localized damage, where the fabric is fixed at all four edges. The same phenomenon is also observed by Shockey et al. [24] when they studied the ballistic performance of one-ply Zylon.

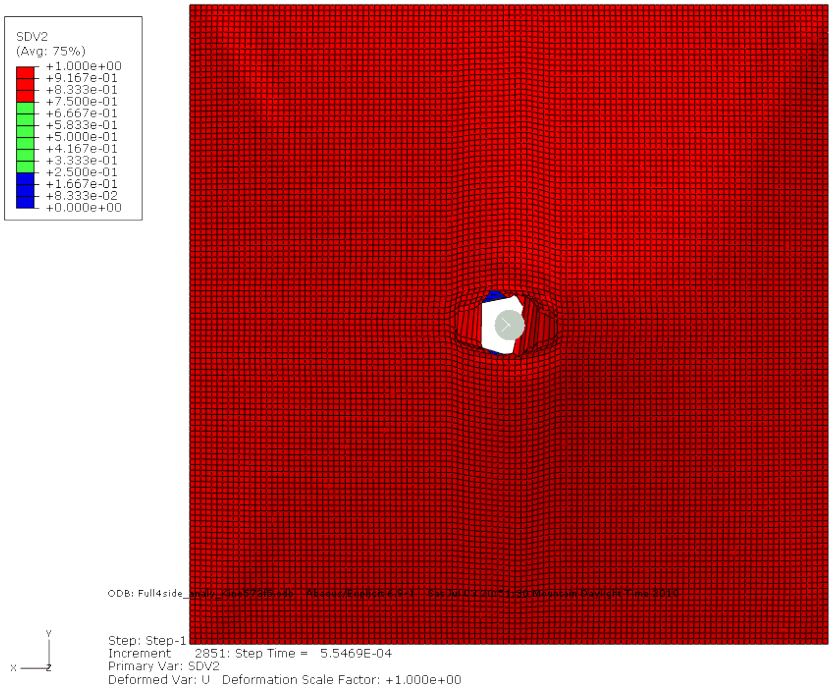

(a) SDV2

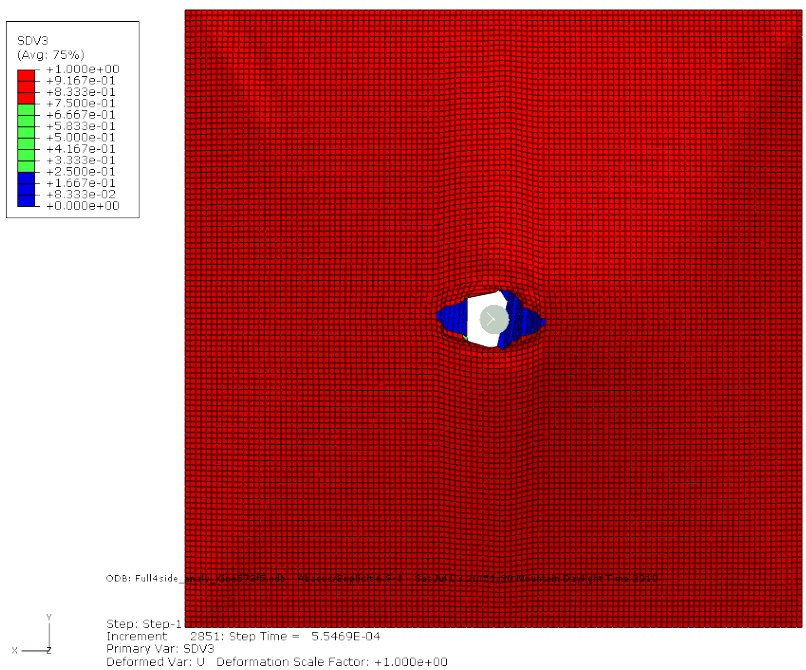

(b) SDV3

Figure 4-9 Damage pattern of four-edge fixed (XY0) friction coefficient = 0.5 and V_0 = 57.3 m/s

The influence of boundary conditions is investigated through study in the resistance forces against the projectile (Figure 4-10). When impacted under the four-edge fixed boundary condition, the fabric is stretched in all directions and once rupture occurs at the impact site, the stretch tension in the fabric enlarges the rupture opening and makes the projectile easily push through the fabric. As shown in Figure 4-10, the fabric is penetrated by the projectile much earlier and faster. However, under two-edge fixed boundary, the projectile is subjected to continuous resistance from the fabric. Therefore, as the underlying reason under four-edge fixed boundary condition, fewer yarns are involved during the impact up to complete damage and less energy is absorbed.

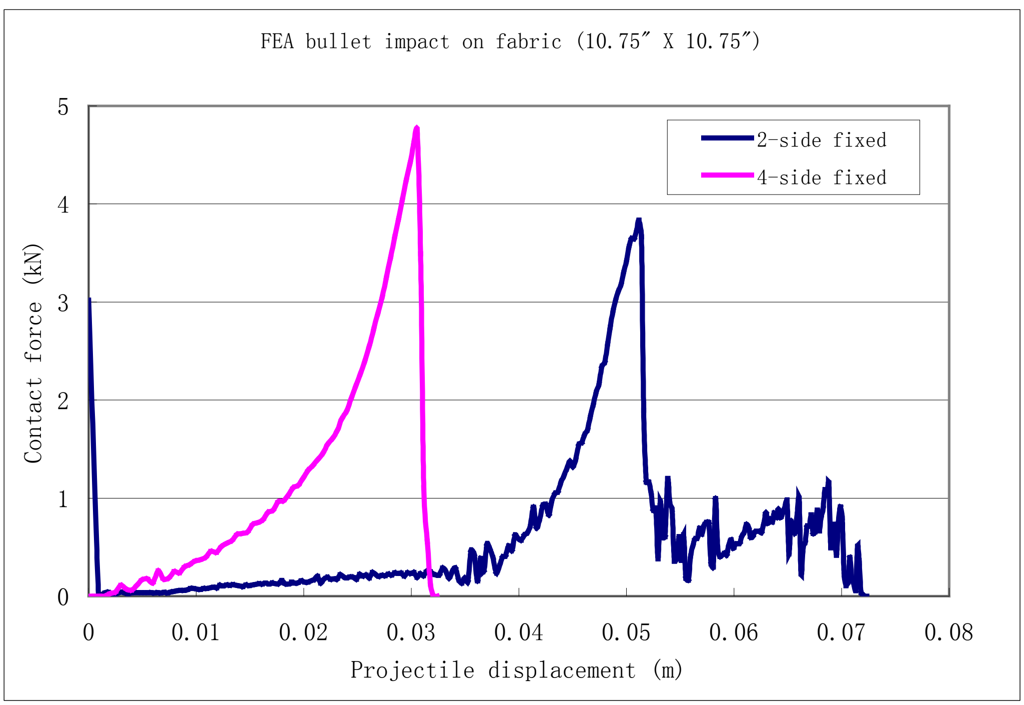

Figure 4-10 Impact force V.S. deflection (V_0 = 57.3)

Under two-edge fixed boundary condition, the fabric can move more freely in both the normal-to-plane direction and the in-plane direction. As indicated by the maximum normal deflection of the fabric under the two kinds of boundary conditions. The maximum fabric deflection is measured at the center of the fabric and at the instant that damage is initiated. As shown in Table 5, the maximum deflection is around 51mm and 26mm for boundary conditions Y90 and XY0, respectively. So, when two edges are fixed, the fabric can acquire higher kinetic energy. The fabric is less constrained to move "following" the projectile and the projectile can not easily push through the fabric. Thus more yarns are involved and damaged. As the result, more energy is absorbed.

Table 5: Effect of boundary conditions on energy absorption (Y90 V.S. XY0)

Initial impact velocity (m/s)		34.5	39.78	57.3	83.06	123.69
Residual velocity (m/s)	Y90	Bounced back	10	32.6	66.83	110
	XY0	13.89	21.82	43.1	71.18	114.9
Projectile energy loss (%)	Y90	100%	93.7%	67.63%	35.3%	20.9%
	XY0	83.8%	69.91%	43.42%	26.93%	13.7%
Absorbed energy (J)	Y90	21.69	27.5	41.19	45.13	59.35
	XY0	18.5	20.52	26.45	33.99	38.9
Max normal deflection (mm)	Y90	50.91	51.85	51.75	51.13	51.25
	XY0	26.5	26.86	27.66	28.26	25.28

Difference in energy absorption is tabulated in Table 5. It is evident that, under the two-edge fixed boundary condition, the fabric absorbs more energy and demonstrates higher projectile-proof performance. The simulation results in Table 5 shows the difference in energy absorption is less than 50%. Similarly, as reported in the ballistic experiment [24], the absorbed energy under two-edge fixed boundary condition is approximately 25% to 60% more for Zylon and almost double for Spectra.

4.4.3 Projectile shapes

Based on the simulations, it is found that the damage manners are also related to the projectile shapes. To show the influence of the projectile shapes, the projectile is filleted. Comparison is made between three simulations as shown in Figure 4-6 (not filleted), Figure 4-11 (0.8mm fillet) and Figure 4-12 (2mm fillet). These three simulations are different because of the sizes of the fillets, which change the sharpness of the projectiles. By comparison, the sharpness of the projectile affects the damage manner significantly and the 0.8mm-filleted projectile (Figure 4-11) causes the most severe and more sites of remote damage.

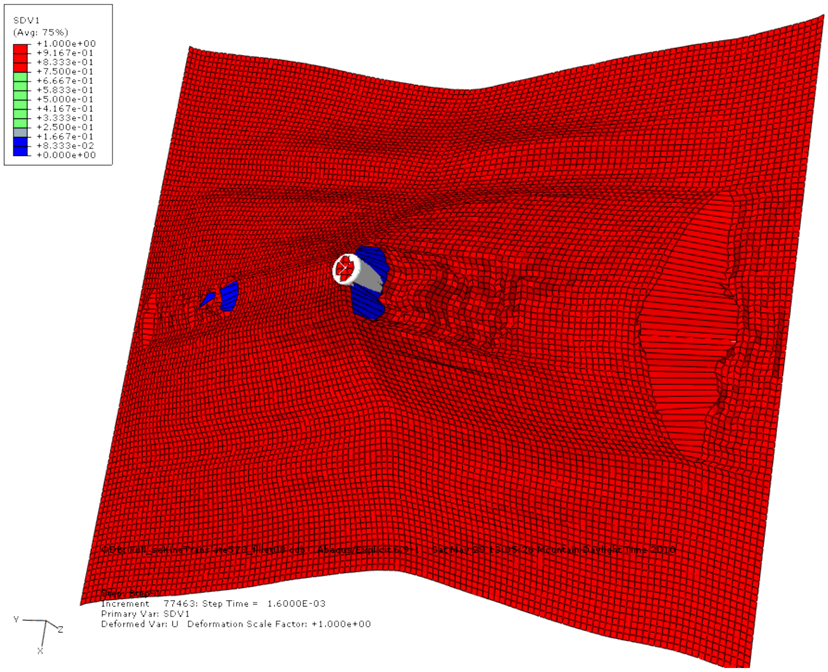

(a) SDV1

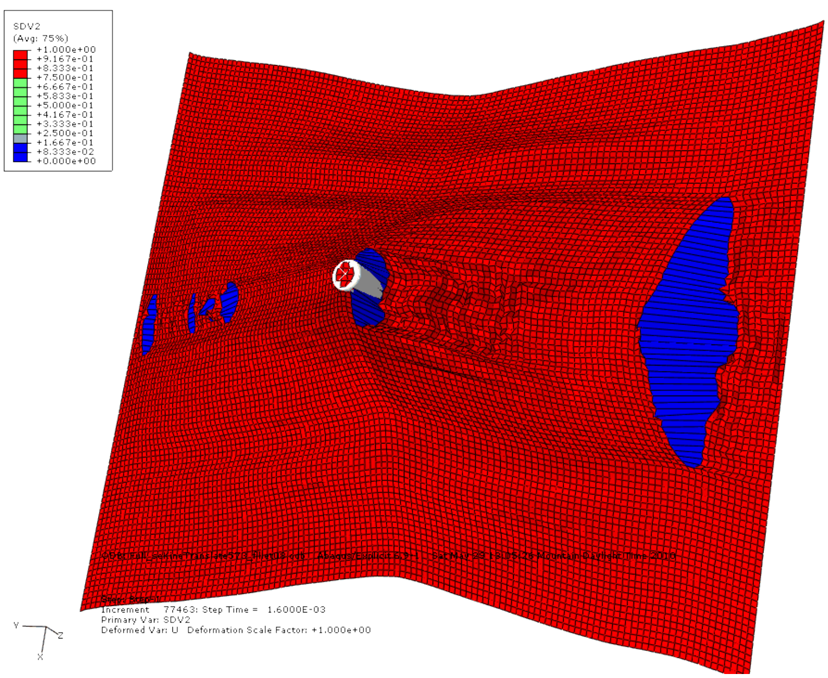

(b) SDV2

Figure 4-11 Damage caused by the filleted projectile

Friction coefficient = 0.5, V_0 = 57.3 m/s (Y90), fillet = 0.8mm

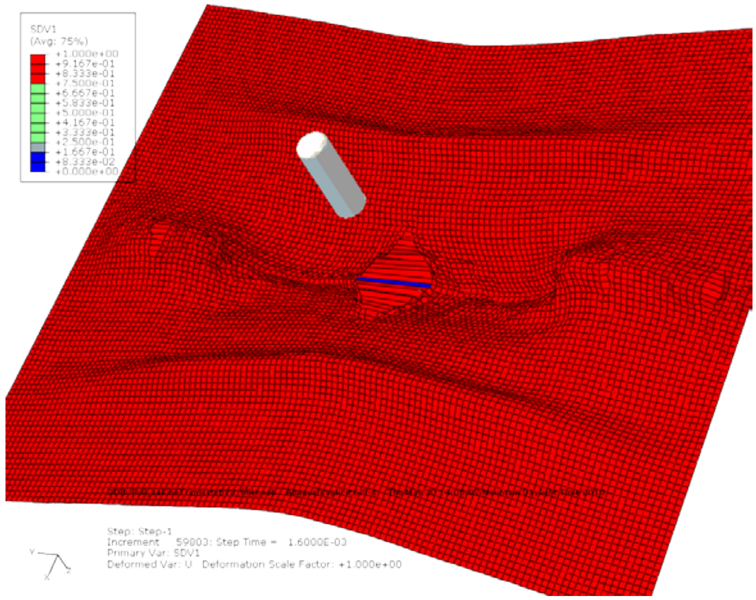

(a) SDV1

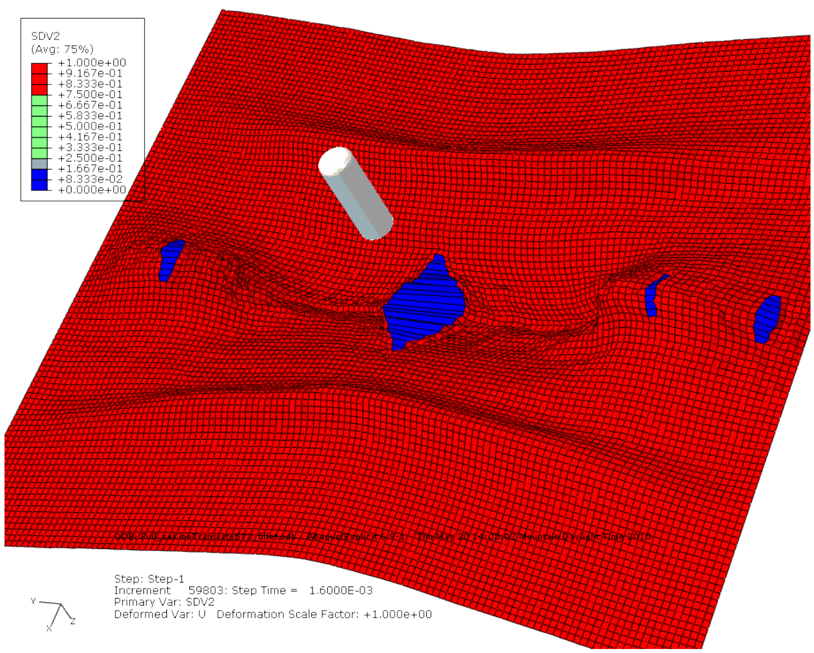

(b) SDV2

Figure 4-12 Damage caused by the filleted projectile

Friction coefficient = 0.5, V_0 = 57.3 m/s (Y90), fillet = 2mm

To relate the sharpness to the damage manners, the sharpness of the projectile is defined based on the energy loss. The projectile is said to be sharper if it causes less energy absorption. The kinetic energy loss of the projectiles is shown in Figure 4-13. According to the comparison, the projectile with 2mm fillet has the highest residual velocity while the one with 0.8mm fillet has the lowest residual velocity. Therefore, the 2mm filleted projectile is the sharpest and the 0.8mm filleted is the bluntest. Based on the determination of the sharpness of the projectiles, it is concluded that the blunt projectile tends to cause remote damage (Figure 4-11).

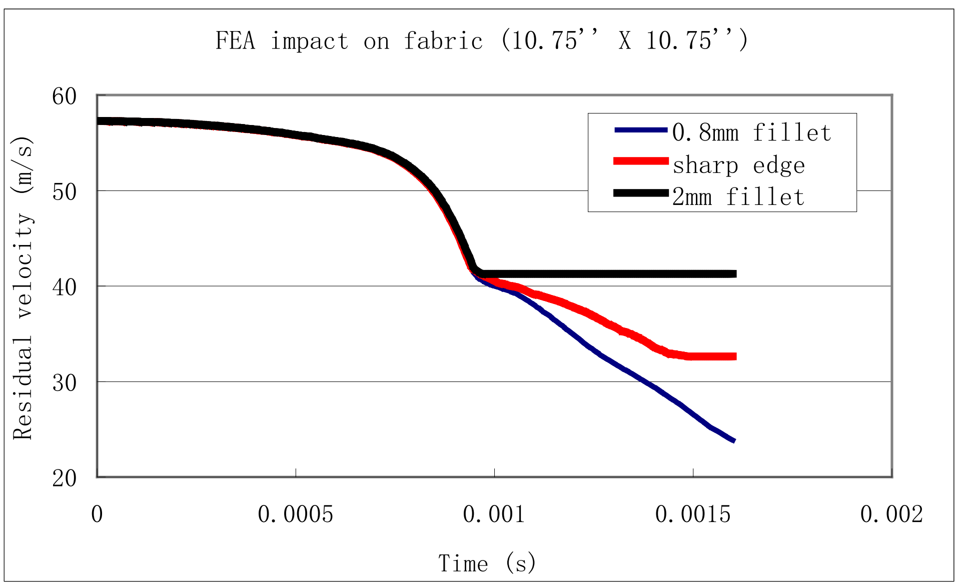

Figure 4-13 Velocity evolution comparison between sharp-edged and filleted projectiles

The underlying reasons can be revealed by referring to Figure 4-14 and by comparing the difference in damage because of the projectile shapes. On one hand, the fillet helps to reduce stress concentration at the direct impact site and this makes the impact loading can be distributed more evenly along the yarns. Consequently, remote damage tends to be caused. On the other hand, the fillet makes it easier for the yarns to slip off the contact end of the projectile and local damage tends to be caused. Which side becomes dominate is determined by the size of the fillet.

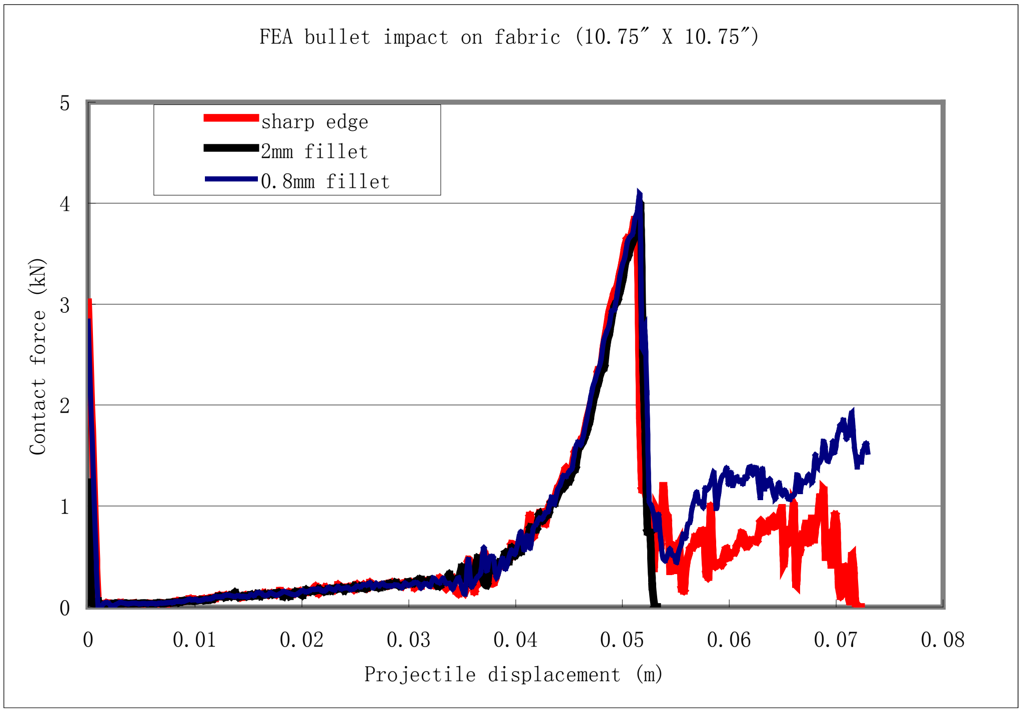

Figure 4-14 Impact force V.S. projectile displacement V_0 = 57.3 (Y90)

Comparison between sharp-edge and filleted projectile

For the 2mm-filleted projectile, the yarns can more easily slip off the head of the projectile and the projectile pushes through the fabric quickly (Figure 4-14). As a result, less fabric material is involved and damaged (Figure 4-12). Damage is mainly caused in warp yarns and complete damage is minor. Consequently the absorbed energy is greatly reduced. The difference is nearly as much as 50% in terms of energy absorption compared with the sharp-edged projectile. For the 0.8mm-filleted projectile, the smaller fillet does not let the projectile push through the fabric as easily as the 2mm fillet. Meanwhile, the smaller fillet greatly reduces the stress concentration. Therefore, the projectile is subjected to continuous resistance. As the result, severe remote damage is caused and more energy is absorbed.

Comparing the 2mm filleted projectile with the sharp-edged projectile, the fillet reduces the stress concentration and thus causes more sites of remote damage (Figure 4-12) than the sharp-edged projectile (Figure 4-6). Because of the sharp edge, stress concentration is incurred and local damage tends to be caused. At the same time, because of the sharp edge, the projectile can not easily pushes through the fabric and, therefore, more material is damaged and more energy is absorbed. This explains the severe remote damage but less energy absorption in Figure 4-12 and, in contrast, the minor remote damage but more energy absorption in Figure 4-6.

Based on the proceeding investigation, it is concluded that blunt projectile tends to cause remote damage and more energy absorption.

4.4.4 Effect of material orientation

Considering the anisotropy property of the fabric materials, the ballistic response is expected to change if the material orientation varies with reference to the fabric fixed edges. To investigate the effect of the material orientation, the fabric is rotated 45° so that both the warp and fill yarns form a 45° angle relative to the edges of the square-shaped fabric. In this section, simulations were implemented with XY45 conditions. The results are compared with the simulations in section 4.4.2, where the fabric is four-edge fixed too, but the material is orientated at 0° (XY0). The only difference in these simulations is material orientation and Table 6 shows the comparison.

Table 6: Effect of material orientation (XY0 V.S. XY45)

Initial impact velocity (m/s)		34.5	39.78	57.3	83.06	123.69
Residual velocity (m/s)	XY45	11.13	19.27	38.5	69.97	113.9
	XY0	13.89	21.82	43.1	71.18	114.9
Projectile energy loss (%)	XY45	89.59%	76.53%	54.85%	29.04%	15.2%
	XY0	83.8%	69.91%	43.42%	26.93%	13.7%
Absorbed energy (J)	XY45	19.78	22.5	33.4	37.16	43.15
	XY0	18.5	20.52	26.45	33.99	38.9
Max normal deflection (mm)	XY45	28.5	28.69	31.63	29.9	26.27
	XY0	26.5	26.86	27.66	28.26	25.28

As shown in Table 6, the residual velocities for XY45 conditions are always lower than XY0 conditions and among the current simulations the difference can be up to 29% in terms of the absorbed energy. This phenomenon indicates that the material orientation affected the ability to arrest the projectile. Hence, the rotated orientation improves the ballistic performance of the fabric. To understand the influence of the material orientation, the following observation is obtained by referring to Figure 4-15 and Figure 4-16, where the stress and strain distribution is shown across the fabric at the instant immediately before the damage initiation. According to the figures, the maximum principal stress and strain are always directed along the warp and fill yarns and their directions rotate following the material orientation. This indicates, with 45° material orientation, the fabric material in diagonal is engaged in resistance against the projectile. Therefore, the rotation of orientation is partially equivalent with increasing the fabric size. For the 45° orientation, the length of the yarns directly engaged in the impact is actually $\sqrt{2}$ times long as the 0° orientation. For this reason, under XY45 conditions, the fabric experiences greater maximum deflection at the center (shown in Table 6) and is able to absorb more energy than 0° orientation.

These simulations alternatively prove that the increased fabric size helps absorb more energy.

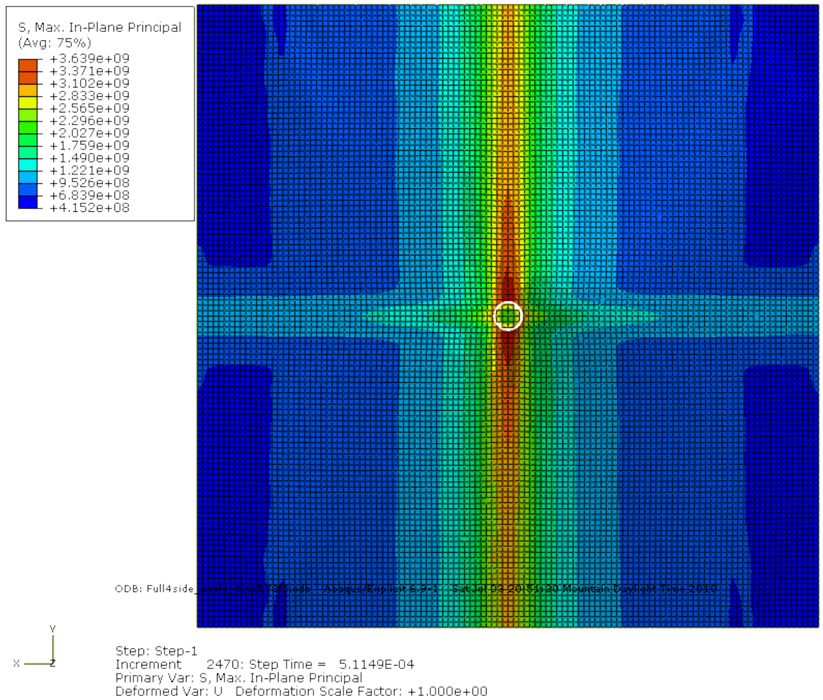

(a) XY0

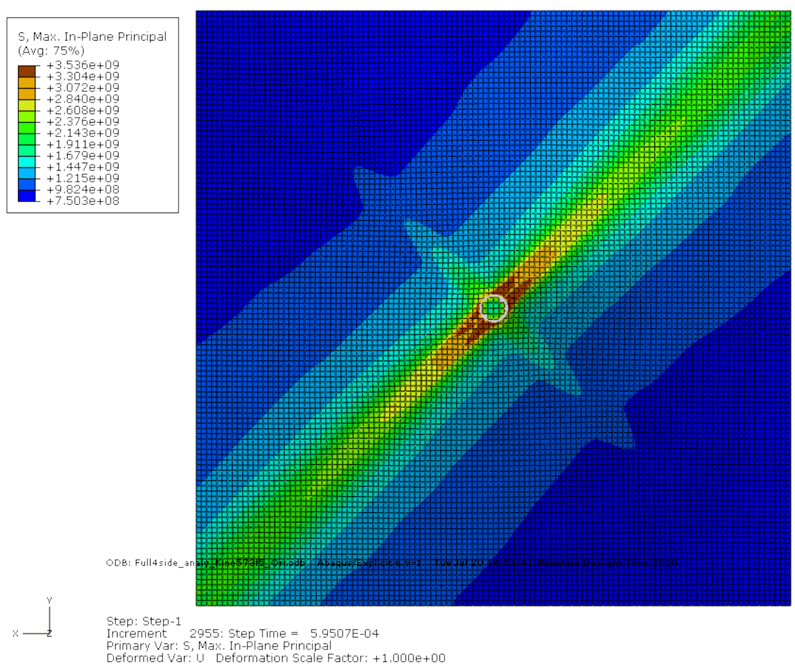

(b) XY45

Figure 4-15 Material orientation effect (V_0 = 57.3 m/s):

Maximum in-plane principal stress

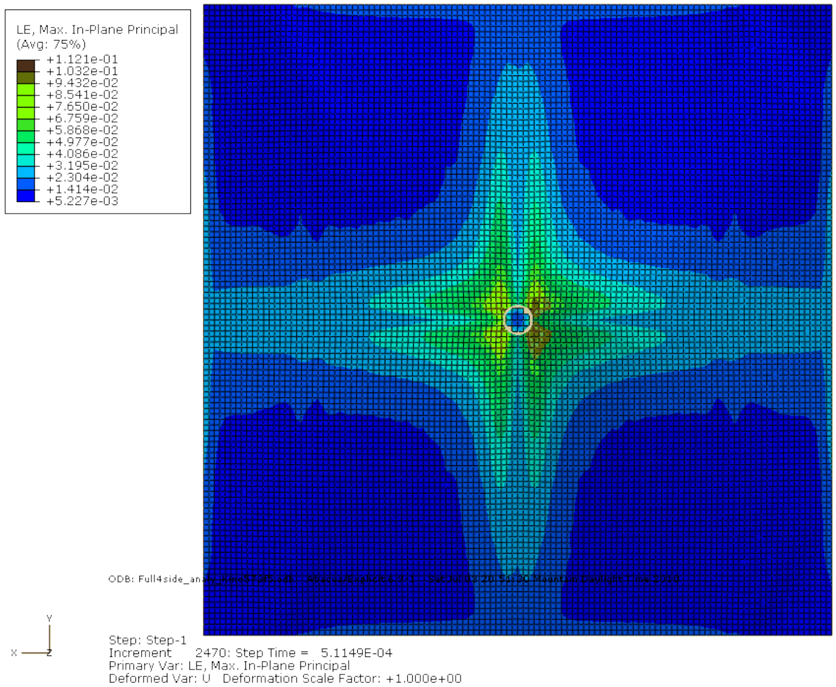

(a) XY0

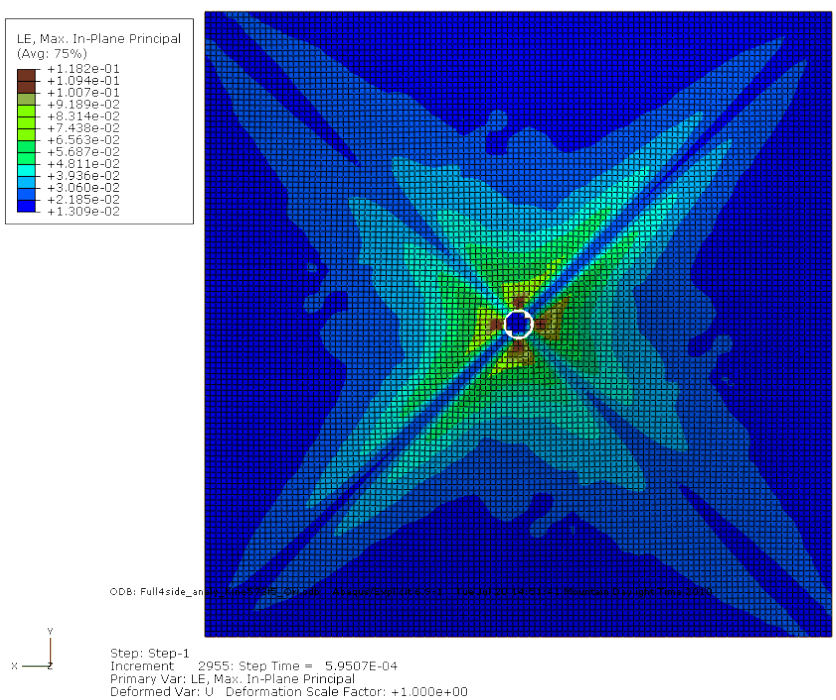

(b) XY45

Figure 4-16 Material orientation effect (V_0 = 57.3 m/s):

Maximum in-plane principal of logarithmic stain

4.4.5 Summary

(1) Summary on damage mechanism

Based on the observation, factors that can reduce stress concentration usually induce remote damage. Conclusions on the influence factors are summarized as follows:

Local failure tends to occur under the following test conditions:

- High level projectile-fabric friction
- Sharper projectiles
- Four-edge gripped fabric

Alternatively, remote failure tends to occur under the conditions:

- Blunt-ended projectile
- Low level friction
- Two-edge gripped fabric

In addition, it is claimed in [24] and [35] that higher impact velocity tends to cause local damage. This is because the viscoelastic property of the material and that high impact velocity breaks the fabric through shearing mechanism instead of stretching. In the current material model, the damage criterion is based on the maximum local stretch of the yarns and is time independent.

(2) Summary on energy absorption

Conditions that allow the fabric to move freely or involve more material help the fabric to store more kinetic and strain energy and absorb more energy. Based on the simulations, the following factors help energy absorption:

- Two-edge fixed boundary condition rather than 4-edge fixed;
- Rotated material orientation;
- Blunt projectile.

Note that inter-yarn friction is another important factor. The friction drags remote material to involve resistance against impact and inter-yarn slipping also dissipates impact energy. The inter-yarn friction is not incorporated in the current material model.

4.5 Directional effect of the yarn weaving structure

The fabric displays anisotropic properties as the result of the weaving structure. Thus directional stress evolution phenomenon occurs. Figure 4-17 shows the directional effect in stress evolution under the two-edge fixed boundary condition (Y90). Although the fabric boundaries are free of constrain in the fill yarn direction, the tension stress is higher in the fill yarns (Figure 4-17(a)) at the early stage of the impact. This is because of higher degree of crimp in warp yarns. Higher degree of crimp makes the warp yarns can be easily straightened up with less resistance than the fill yarns. For the same reason, the stress wave travels faster in the fill yarns at the early stage. As the result, when the stress wave in fill yarns reaches the boundary and has been reflected, the stress wave front in warp yarns has not reached the boundary yet (Figure 4-17 (b)). With impacting continued, stretch resistance from warp yarns increases rapidly due to the fixed boundaries in the warp direction. At the moment shown in Figure 4-17 (c), tension stress in warp yarns becomes greater than that in fill yarns. At the moment shown in Figure 4-17 (d), tension stress is dominantly localized in the warp direction.

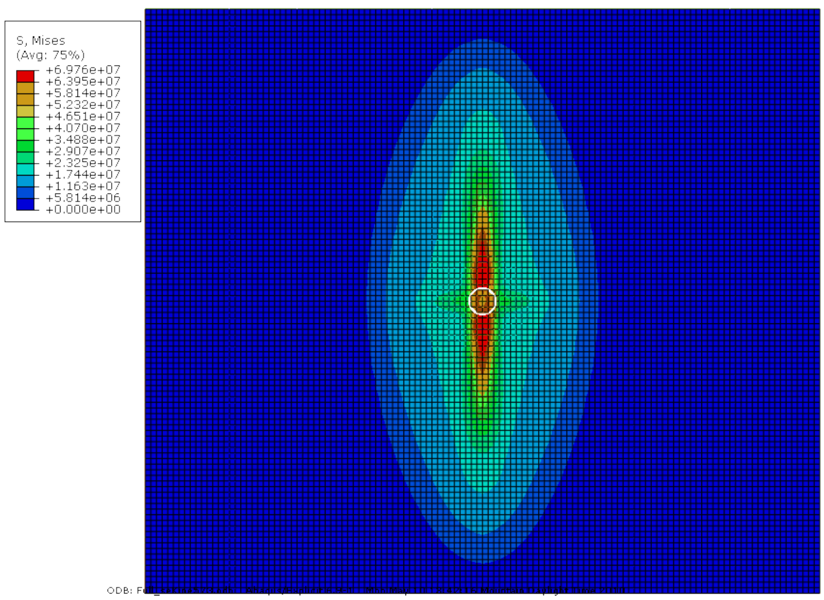

(a) time(s): 1.6058E-05

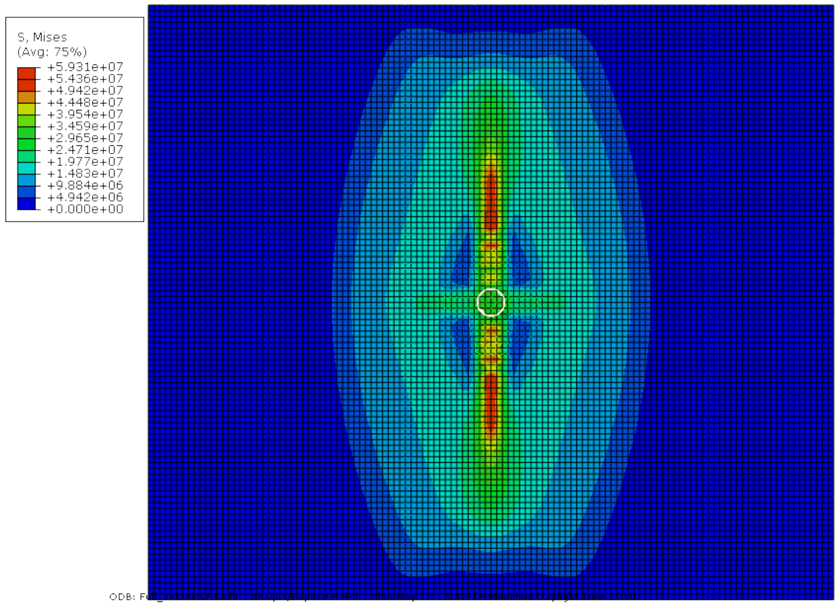

(b) time(s): 3.21117E-05

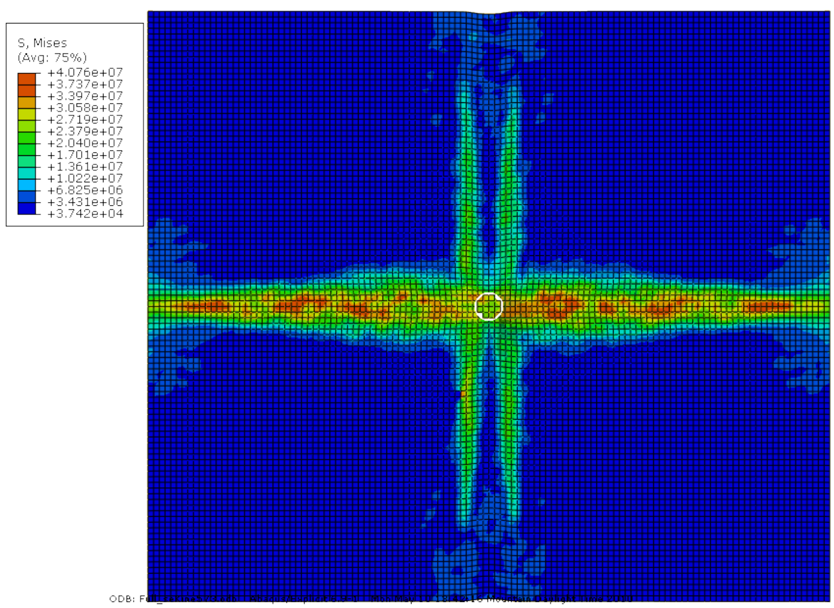

(c) time(s): 8.5353E-05

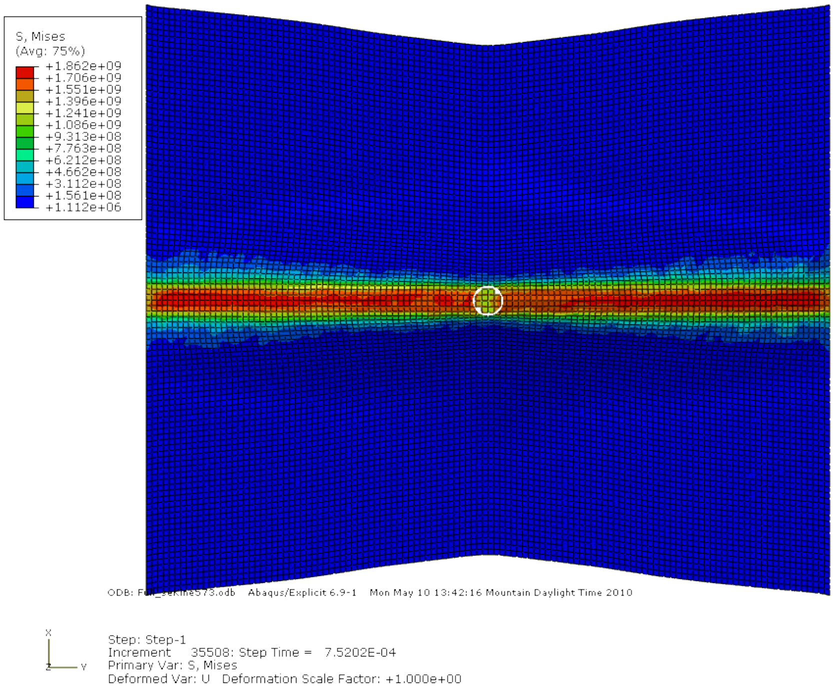

(d) time(s): 8.9067E-04

Figure 4-17 Yarn weaving directional effect study (Y90):
stress wave evolution during ballistic impact

Similarly, the study of stress evolution is repeated for the four-edge-fixed boundary condition (XY0). As shown in Figure 4-18, because of the anisotropy of the fabric material, the stress distribution is not axially symmetric with respect to the impact direction. By comparison with the Y90 boundary condition, the same stress distribution is observed between them at the early stage. In both cases (Figure 4-18(a) and Figure 4-17(a)), the tension stress is higher in the fill direction and the stress wave travels faster in the fill direction due to the lower degree of crimp in fill yarns. Therefore, at the early stage, the fabric response is mainly determined by yarn crimp instead of the boundary conditions. When the impact process continues, the difference appears because of the different boundary conditions. Under Y90 boundary condition (Figure 4-17), the stress in fill yarns gradually diminishes while the stress in warp yarns increases continuously. Under XY0 boundary condition (Figure 4-18), the stress keeps increasing in both directions and higher stress level in fill yarns before damage.

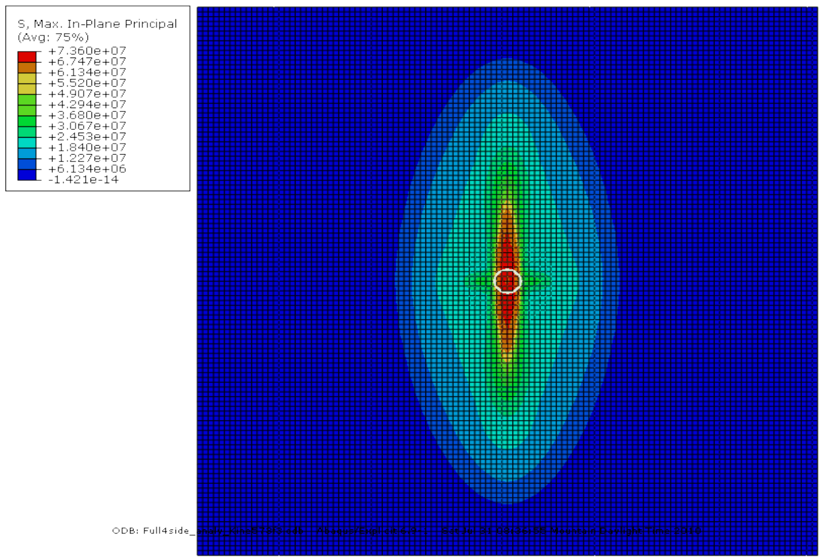

(a) time(s): 1.5121E-05

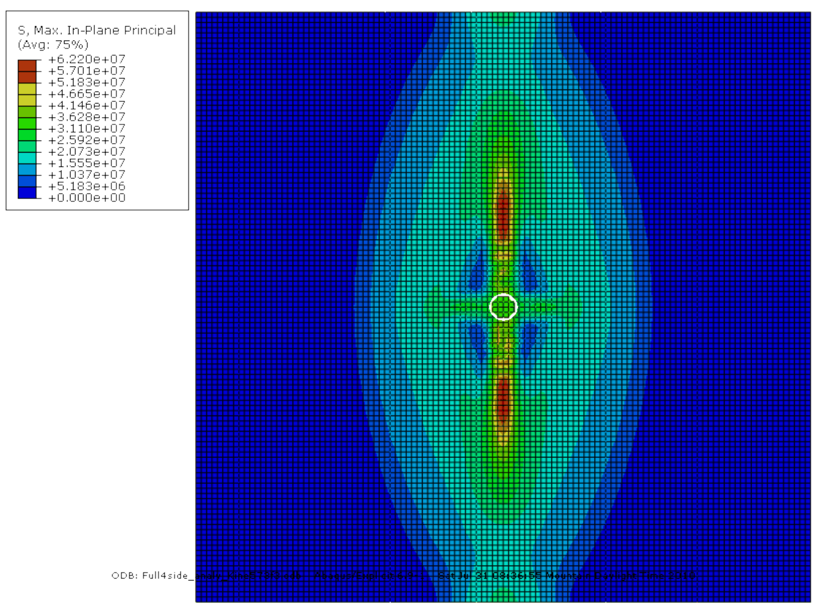

(b) time(s): 2.0029E-05

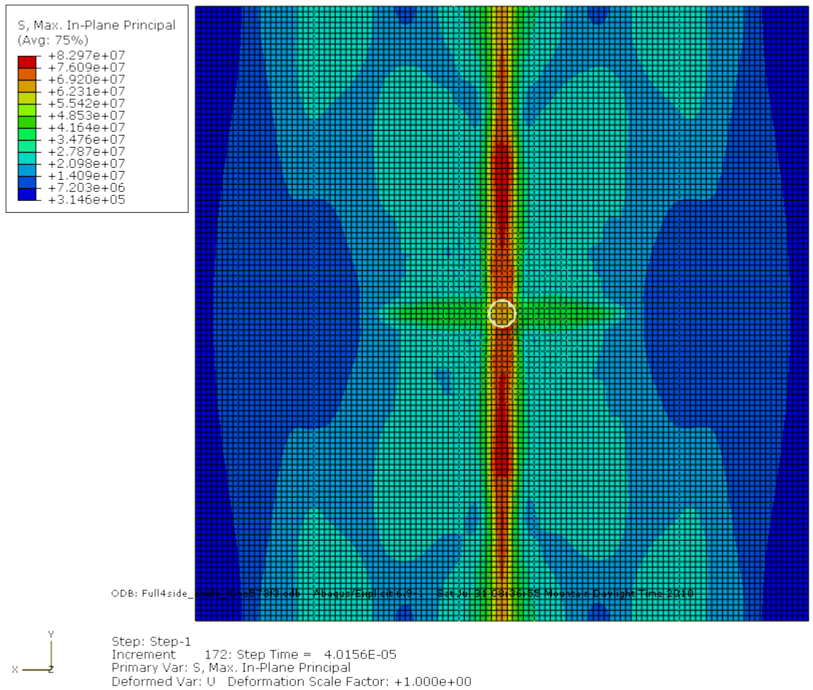

(c) time(s): 4.0156E-05

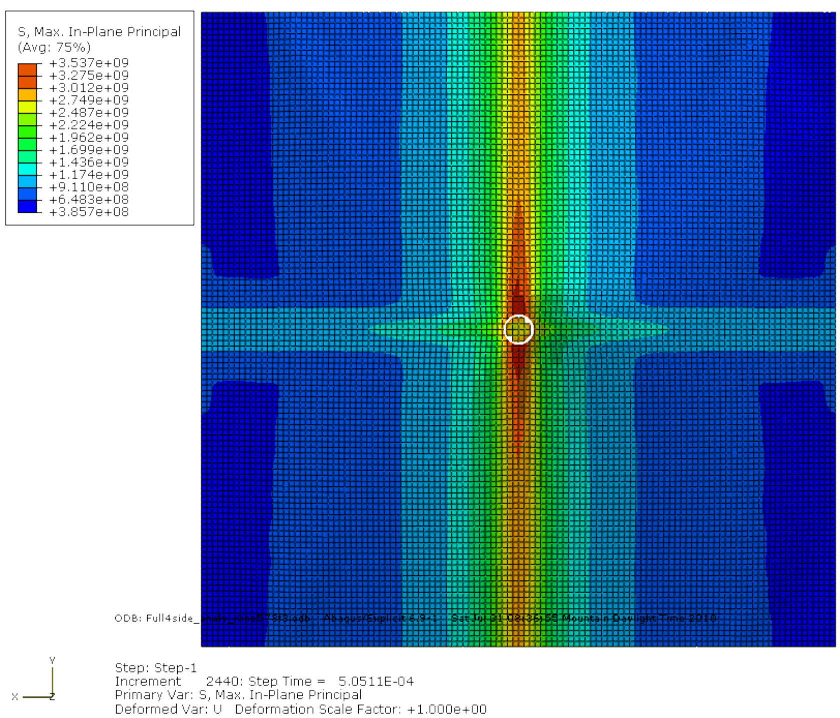

(d) time(s): 5.0511E-04

Figure 4-18 Yarn weaving directional effect study (XY0): stress wave evolution during ballistic impact

Chapter 5

Conclusions

The current work proposed a multi-scale model for plain woven fabric materials. This material model considers both the membrane-like properties and the underlying sub-structures of the fabric materials. On the top scale, the fabric is assumed as a membrane with no out-of-plane bending and shearing stiffness. Following are the yarn scale and fibril scale, which reflect the yarn weaving structure and material composition details.

Static and dynamic numerical simulations were performed with this multi-scale material model. The results demonstrated that the material model is able to reflect complicated characteristics of the fabric materials. Various physical phenomena can be observed in the simulations with variation of impact conditions. The simulation results also show good agreement experimental data.

It is found that the ballistic performance and mechanical response of the fabric materials are determined by a combination of a variety of factors and conditions rather than the material properties alone. The material properties are the underlying base reflecting strength of the fabric. However the fabric is a structural assembly of the fibrous materials and the fabric weaving structure. Boundary conditions and material orientation also play important roles and significantly influence the ballistic performance.

5.1 Abilities of the model

- Weaving structure and interaction between yarns

Weaving structure includes the yarn crimping, number of yarns per length and weaving geometry. This is the inherent origin of various unique features of the fabric material rather than continuum membrane.

- Material anisotropy

Anisotropy is an important feature of the fabric and is attributed to a number of unique phenomena of the fabric materials such as channelling stress distribution, directional effect of stress wave propagation, pyramid-shape deformation.

- Gradual damage in the fabric

By tracking the current and history maximum local stretch of the yarns, the damage status of the fabric is monitored and updated. The model considers the misalignment of fibrils in the yarn, thus the gradual damage in the material is reflected.

5.2 Deficiencies of the model

- Damage criterion

The damage criterion of the current model is based on yarn stretch and is time independent. In fact, yarns are viscoelastic and the critical stretch should be reduced with increasing impact velocities. In addition, high level impact velocity can damage the fabric by a shearing mechanism. It is observed in experiment that the energy absorption decreases when the impact velocity is beyond a certain value.

- Inter-yarn relative slipping

The current model allows inter-yarn rotation but not for inter-yarn slipping. Thus phenomena like yarn pull-out failure and inter-yarn friction can not be simulated.

5.3 Findings and observations

Based on the simulations, there are the following findings and conclusions, which agree with published experimental data.

- Energy absorption

Energy absorption is increased with the two-edge fixed boundary condition in contrast to the four-edge fixed boundary condition. More energy is absorbed when the material orientation is rotated with reference to the fixed edges. The rotation actually increases the length of material engaged during the impact. This is partially equivalent to increasing the fabric size. Blunt projectile involves more materials and tends to cause more severe and extensive damage, which leads to more energy absorption.

- Damage modes

Local and remote damage is observed as the two damage mode in the simulations. Yarn pull-out failure due to inter-yarn slipping is another damage mode that can be observed in experiment but not in the current simulations. Based on these simulations, it is found that four-edge fixed boundary condition, sharp projectile and high level projectile-fabric friction tend to cause local damage.

Bibliography

[1] Vinson, J. R., and Zukas, J. A., 1975, "On the Ballistic Impact of Textile Body Armor," ASME J. Appl. Mech., 42(6), pp. 263-268.

[2] Phoenix, L. S., and Porwal, P. K., 2003, "A New Membrane Model for the Ballistic Impact Response and V50 Performance of Multi-Ply Fibrous Systems," Int. J. Solids Struct., 40, pp. 6723-6765.

[3] Gu, B., 2003, "Analytical Modeling for the Ballistic Perforation of Planar Plain-Woven Fabric Target by Projectile," Composites, Part B, 34B(4), pp. 361-371.

[4] Billon, H. H., and Robinson, D. J., 2001, "Models for the Ballistic Impact of Fabric Armor," Int. J. Impact Eng., 25, pp. 411-422.

[5] Cunniff, P. M., 1996, "A Semi-empirical Model for the Ballistic Impact Performance of Textile-Based Composites," Text. Res. J., 66, pp. 45-59.

[6] Shim, V. P. W., Lim, C. T., and Foo, K. J., 2001, "Dynamic Mechanical Properties of Fabric Armor," Int. J. Impact Eng., 25, pp. 1-15.

[7] Gu, B., 2004, "Ballistic Penetration of Conically Cylindrical Steel Projectile Into Plain-Woven Fabric Target: A Finite Element Simulation," J. Compos. Mater., 38(22), pp. 2049-2074.

[8] Taylor, W. J., and Vinson, J. R., 1990, "Modeling Ballistic Impact Into Flexible Materials," AIAA J., 28(2), pp. 2098-2103.

[9] Shim, V. P. W., Tan, V. B. C., and Tay, T. E., 1995, "Modeling deformation and Damage Characteristics of Woven Fabric Under Small Projectile Impact," Int. J. Impact Eng., 16(4), pp. 585-605.

[10] Zohdi, T., Powell, D., 2006, "Multiscale Construction and Large-scale Simulation of Structural Fabric Undergoing Ballistic Impact," Comput. Mechods. Appl. Mech. Eng., 195, pp 94-109.

[11] Ivanov, I., and Tabiei, A., 2004, "Loosely Woven Fabric Model With Viscoelastic Crimped Fibers for Ballistic Impact Simulations," Int. J. Numer. Methods Eng., 61, pp. 1565-1583.

[12] Ting, C., Ting, J., Roylance, D., Cunniff, P., 1998, "Numerical Characterization of the Effects of Transverse Yarn interaction on Textile Ballistic Response," 30th International SAMPE Technical conference, pp 57-67.

[13] King, M.J., Jearanaisilawong, P. and Socrate, S., 2005, “A Continuum Constitutive Model for the Mechanical Behavior of Woven Fabrics,” Int. J. Solids Struct., 42, pp 3867-3896.

[14] Nadler, B., Papadopoulos, P. Steigmann, D., 2006, “Multiscale Constitutive Modeling and Numerical Simulation of Fabric Material,” Int. J. Sol. Stru., 43, pp 206-221.

[15] Lim, C. T., Shim, V. P. W., and Ng, Y. H., 2003, “Finite-Element Modeling of the Ballistic Impact of Fabric Armor,” Int. J. Impact Eng., 28, pp. 13-31.

[16] Cunniff, P. M., and Ting, J., 1999, “Development of a Numerical Model to Characterize the Ballistic Behavior of Fabrics,” 18th International Symposium on Ballistics, San Antonio, TX, pp. 822-828.

[17] Johnson, G. R., Beissel, S. R., and Cunniff, P. M., 1999, “A Computational Model for Fabric Subjected to Ballistic Impact,” Proceedings of the 18th International Symposium on Ballistics, San Antonio, TX.

[18] Zeng, X. S., Tan, V. B. C., Shim, V. P. W., 2006, "Modelling Inter-yarn Friction in Woven Fabric Armour", Int. J. Numer. Meth. Eng., 66, pp 1309-1330

[19] Duan, Y., Keefe, M., and Bogetti, T. A., Powers, B., 2006, "Finite Element Modeling of Transverse Impact on a Ballistic Fabric," Int. J. Mech. Sci., 48, pp. 33-43.

[20] Duan, Y., Keefe, M., and Bogetti, T. A., Cheesemanc, B.A., Powersc, B., 2006, "A Numerical Investigation of the Influence of Friction on the Energy Absorption by a High-Strength Fabric Subjected to Ballistic Impact," Int. J. Impact Eng., 32, pp. 1299-1312.

[21] Duan, Y., Keefe, M., and Bogetti, T. A., Cheeseman, B. A., 2005, "Modeling the Role of Friction During Ballistic Impact of a High-Strength Plain-Weave Fabric," Compos. Struct., 68, pp. 331-337.

[22] Shockey, D. A., Erlich, D. C., and Simons, J. W., 1999, "Improved Barriers to Turbine Engine Fragments: Interim Report I," Report No. DOT/FAA/AR-99/8,I.

[23] Shockey, D. A., Erlich, D. C., and Simons, J. W., 1999, "Improved Barriers to Turbine Engine Fragments: Interim Report II," Report No. DOT/FAA/AR- 99/8, II.

[24] Shockey, D. A., Erlich, D. C., and Simons, J. W., 2004, “Improved Barriers to Turbine Engine Fragments: Interim Report III,” Report No. DOT/FAA/AR-99/8, III.

[25] Shockey, D. A., Erlich, D. C., and Simons, J. W., 2002, “Improved Barriers to Turbine Engine Fragments: Interim Report IV,” Report No. DOT/FAA/AR- 99/8, IV.

[26] Shockey, D. A., Erlich, D. C., and Simons, J. W., 2002, “Improved Barriers to Turbine Engine Fragments: Final Annual Report,” Report No. DOT/FAA/AR-99/8, V.

[27] Antman, S., 1968, “General Solutions for Plane Extensible Elasticae Having Nonlinear Stress-strain Laws,” Quarterly of Applied Mathematics, 26(1), pp 35-47.

[28] Warren, W., 1992, “The Large Deformation Elastic Response of Woven Kevlar Fabric,” Polymer Composites, 13(4), pp 278-284.

[29] Toyobo Co., Ltd., 2005 (Revised), “PBO Fiber Zylon Technical Information”, Website: www.toyobo.co.jp

[30] Zohdi, T. I., Steigmann, D. J., 2002, “The Toughening Effect of Microscopic filament misalignment on macroscopic ballistic fabric response,” Intl. J. Fract, 118, pp L71-76.

[31] Verzemnieks, J. in Boeing Company, 2005. “Lightweight Ballistic Protection of Flight-critical Components on Commercial Aircraft, Part 3: Zylon yarn tests”, Report No.: DOT/FAA/AR-05/45, P3

[32] Arizona State University, 2004. “Explicit Finite Element Modeling of Multilayer Composite Fabric for Gas Turbine Engine Containment Systems, Part 1: static tests and modeling”, Report No.: DOT/FAA/AR-04/40, P1

[33] Ericksen, R.H., Warren, W., 1992, “Deflection-force Measurements and Observations on Kevlar 29 Parachute Fabrics,” Textile Research Journal, 62(11), pp 628-637.

[34] Rebouillat, S., 1998, “Tribological properties of woven para-aramid fabrics and their constituent yarns”, J. Mater. Sci., 33, pp3293-3301.

[35] Tan, V. B. C., Lim, C. T., and Cheong, C. H., 2003, “Perforation of High-Strength Fabric by Projectiles of Different Geometry,” Int. J. Impact Eng., 28, pp. 207-222.

Appendix:
Numerical algorithm and procedure

A.1 Algorithm flowchart

The following flow chart describes the procedure used to solve the governing equations of the fabric material model. As shown in the following flow chart, A_1^0, A_2^0, B_1^0, B_2^0 are the initial stiffness of the yarns before damage; α_1^0, α_2^0 are the guess values used at the beginning of the numerical procedure. The input values are the current stiffness A_1, A_2, B_1, B_2 and the membrane Lagrangian strains E_1, E_2. By employing the tools of weak formulation and one dimensional finite element method, the solutions of unknowns are the external forces, F_1, F_2, the inter-yarn contact force, V, the current yarn angle, ϕ, and the yarn maximum local stretch μ_1, μ_2.

Since the yarn damage is controlled by the maximum local stretch, α_1, α_2 have to match corresponding μ_1, μ_2 to be an acceptable set of solutions. Secant method is used for iterating α_1, α_2.

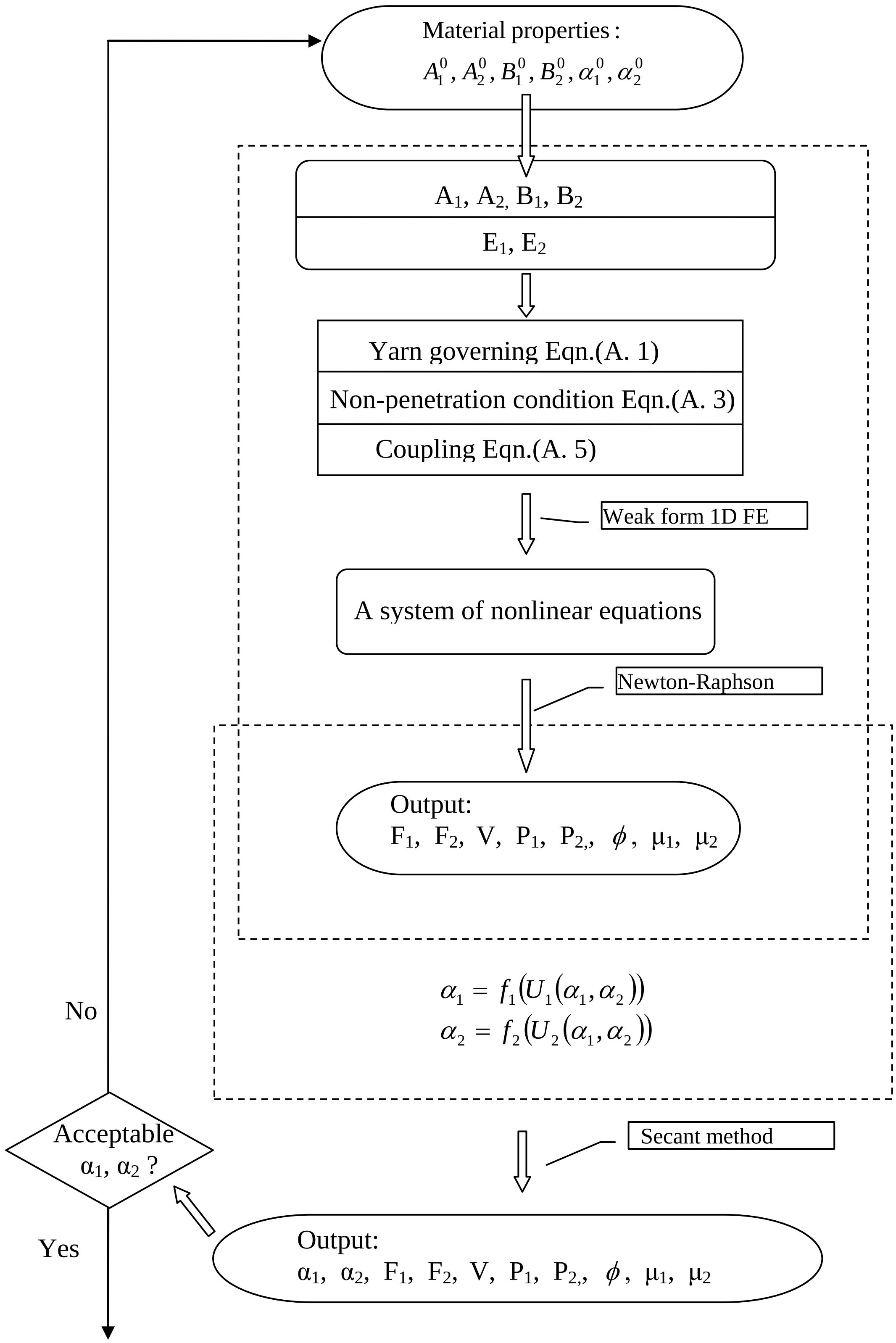
Material properties :
$A_1^0, A_2^0, B_1^0, B_2^0, \alpha_1^0, \alpha_2^0$
A_1, A_2, B_1, B_2
E_1, E_2
Yarn governing Eqn.(A. 1)
Non-penetration condition Eqn.(A. 3)
Coupling Eqn.(A. 5)
Weak form 1D FE
A system of nonlinear equations
Newton-Raphson
Output:
F_1, F_2, V, P_1, P_2, ϕ, μ_1, μ_2
$\alpha_1 = f_1(U_1(\alpha_1, \alpha_2))$
$\alpha_2 = f_2(U_2(\alpha_1, \alpha_2))$
Secant method
No
Acceptable
α_1, α_2 ?
Yes
Output:
α_1, α_2, F_1, F_2, V, P_1, P_2, ϕ, μ_1, μ_2

A.2 Numerical procedure

The differential equation to be solved for F_i and V:

$$\frac{d}{dS}\left\{B_i \frac{d}{dS}\left[\phi_i(S)-\Phi_i(S)\right]\right\}\left[1+\frac{N_i(S)}{A_i}\right]^{-1}=Q_i(S) \qquad (1)$$

$$N_i(S)=F_i\cos\phi_i(S)+V\sin\phi_i(S) \qquad (2)$$

$$Q_i(S)=V\cos\phi_i(S)-F_i\sin\phi_i(S) \qquad (3) \qquad \text{(A. 1)}$$

Note that in Eqn. (A. 1) and the following formulations i = 1, 2, which indicate the warp and fill yarns, respectively. These equations are not summed over i.

Boundary conditions associated with Eqn. (A. 1):

$$\begin{aligned} &\text{BC1:} \quad \phi_i(0)=0 \\ &\text{BC2:} \quad \frac{d}{dS}[\phi_i(S)-\Phi_i(S)]=0 \end{aligned} \qquad \text{(A. 2)}$$

Non-penetration constrain condition:

$$D=D_1+D_2, \qquad \begin{cases} D=0, & \text{yarn in contact} \\ D>0, & \text{yarn in separation} \end{cases} \qquad \text{(A. 3)}$$

where the D_1 and D_2 are the displacements of the two points on the warp and fill yarns, where BC1 is located by referring to Figure 2-4 and,

$$D_i = \int_0^{L_i} \left[\left(1 + \frac{N_i(S)}{A_i} \right) \sin \phi_i(S) - \sin \Phi_i(S) \right] dS \, . \tag{A. 4}$$

D is the summation of D_1 and D_2. $D > 0$ denotes that the warp and fill yarns are separate from each other. The contact constraint condition is thus deactivated and the contact force vanishes (i.e $V = 0$). Otherwise, $D = 0$ indicates the two yarns are in contact and the constraint condition $D = 0$ applies. $D < 0$ is not allowed since the negative value means the two yarns penetrate each other.

Coupling condition:

$$\sqrt{1 + 2E_i} \int_0^{L_i} \cos \Phi_i(S) dS = \int_0^{L_i} \left[\left(1 + \frac{N_i(S)}{A_i} \right) \cos \phi_i(S) \right] dS \tag{A. 5}$$

Eqn. (A. 5) couples the membrane scale and the yarn scales. The left-hand side of Eqn. (A. 5) computes the length of the membrane segment in the deformed configuration. The right-hand side computes the yarn dimension projected to the membrane tangent plane. So, Eqn. (A. 5) sets up the connection and unifies the two separate scales through the deformation kinematics.

Based on the 1-D finite element method, the yarn governing equilibrium equation (Eqn. A. 1) can be rewritten as

$$\begin{aligned}&\frac{d}{dS}\left[TB_i\frac{d}{dS}(\phi(S)-\Phi(S))\right]-\left(\frac{dT}{dS}\right)\left[B_i\frac{d}{dS}(\phi(S)-\Phi(S))\right]\\&=-T\left[-F_i\sin\phi(S)+V\cos\phi(S)\right]\left[1+\frac{1}{A_i}(F_i\cos\phi(S)+V\sin\phi(S))\right]\end{aligned} \tag{A. 6 }$$

where T is introduced as the test function,

$$T=\sum_{k=1}^{n+1}a_k\varphi_k(S) \tag{A. 7}$$

and the yarn angles $\phi_i(S)$ is approximated as

$$\phi_i(S)\approx\sum_{j=1}^{n+1}b_j^i\varphi_j(S). \tag{A. 8}$$

Based on the weak formulation, the left-hand side of Eqn. (A.6) becomes

$left\_side$

$$= \int_0^L \frac{d}{dS}\left[\left(\sum_{k=1}^{n+1} a_k\varphi_k\right) B_i \frac{d}{dS}\left(\sum_{j=1}^{n+1} b_j^i\varphi_j - \Phi\right)\right] dS - \int_0^L \left[\frac{d}{dS}\left(\sum_{i=1}^{n+1} a_k\varphi_k\right) B_i \frac{d}{dS}\left(\sum_{j=1}^{n+1} b_j^i\varphi_j - \Phi\right)\right] dS$$

$$= \left[\left(\sum_{k=1}^{n+1} a_k\varphi_k\right) B_i \frac{d}{dS}\left(\sum_{j=1}^{n+1} b_j^i\varphi_j - \Phi\right)\right]_0^L - \left(\int_0^L \left[\left(\sum_{k=1}^{n+1} a_k \frac{d\varphi_k}{dS}\right) B_i \left(\sum_{j=1}^{n+1} b_j^i \frac{d\varphi_j}{dS} - \frac{d\Phi}{dS}\right)\right] dS\right)$$

$$= \sum_{k=1}^{n+1} a_k \left[\varphi_k B_i \left(\sum_{j=1}^{n+1} b_j^i \frac{d\varphi_j}{dS} - \frac{d\Phi}{dS}\right)\right]_0^L - \sum_{i=1}^{n+1} a_i \left(\int_0^L \left[\frac{d\varphi_k}{dS} B_i \left(\sum_{j=1}^{n+1} b_j^i \frac{d\varphi_j}{dS} - \frac{d\Phi}{dS}\right)\right] dS\right)$$

$$= 0 - \sum_{k=1}^{n+1} a_k \left(\int_0^L \left[\frac{d\varphi_k}{dS} B_i \left(\sum_{j=1}^{n+1} b_j^i \frac{d\varphi_j}{dS} - \frac{d\Phi}{dS}\right)\right] dS\right)$$

In the left hand side shown above, the first integration always vanishes because of the boundary condition BC2 in Eqn. (A. 12) and that the test function (Eqn. A. 7) is chosen such that it vanishes at boundary BC1. The right-hand side of Eqn. (A. 6) becomes

$right\_side$

$$= -\sum_{k=1}^{n+1} a_k \int_0^L \varphi_k \left[F_i \sin\left(\sum_{j=1}^{n} b_j^i\varphi_j\right) + V\cos\left(\sum_{j=1}^{n} b_j^i\varphi_j\right)\right]\left[1 + \frac{1}{A_i} F_i \cos\left(\sum_{j=1}^{n+1} b_j^i\varphi_j\right) + V\sin\left(\sum_{j=1}^{n+1} b_j^i\varphi_j\right)\right] dS$$

So Eqn. (A. 6) becomes

$$-\sum_{k=1}^{n+1} a_k \int_0^L \left[\frac{d\varphi_k}{dS} B_i \left(\sum_{j=1}^{n+1} b_j^i \frac{d\varphi_j}{dS} - \frac{d\Phi}{dS}\right)\right] dS =$$

$$-\sum_{k=1}^{n+1} a_k \int_0^L \varphi_k \left[-F_i \sin\left(\sum_{j=1}^{n+1} b_j^i\varphi_j\right) + V\cos\left(\sum_{j=1}^{n+1} b_j^i\varphi_j\right)\right]\left[1 + \frac{1}{A_i}\left(F_i \cos\left(\sum_{j=1}^{n+1} b_j^i\varphi_j\right) + V\sin\left(\sum_{j=1}^{n+1} b_j^i\varphi_j\right)\right)\right] dS$$

(A.9)

Since a_k are arbitrary and Eqn. (A. 9) is always valid it must be always true that

$$\int_0^L \left[\frac{d\varphi_k}{dS} B_i \left(\sum_{j=1}^{n+1} b_j^i \frac{d\varphi_j}{dS} - \frac{d\Phi}{dS} \right) \right] dS$$
$$= \int_0^L \varphi_k \left[-F_i \sin\left(\sum_{j=1}^{n+1} b_j^i \varphi_j \right) + V \cos\left(\sum_{j=1}^{n+1} b_j^i \varphi_j \right) \right] \left[1 + \frac{1}{A_i} \left(F_i \cos \sum_{j=1}^{n+1} b_j^i \varphi_j + V \sin \sum_{j=1}^{n+1} b_j^i \varphi_j \right) \right] dS$$

(A. 10)

Eqn. (A. 10) is a system of k equations, and for each specific value of the integer k, it constitutes one equation. So, based on the weak formulation and the 1-D finite element method, the yarn governing equation (Eqn. A.1) is converted into a system of k equations. The number of equations is determined by the number of elements (n=k-1) used to approximate the yarn angles (Eqn. A. 10). Also, there is one constraint equation (Eqn. A. 3) and the two coupling equations (Eqn. A. 5). The current model is converted to a problem of solving a system of (3 + 2k) equations with the unkowns F_1, F_2, V, b_j^1 and b_j^2. It is chosen that $k = j$. The system of equations is solved through Newton-Raphson method.

The damage in the fabric is monitored via the maximum local stretch of the yarns. The yarn local stretch is computed by

$$\mu_i(S) = 1 + \frac{N_i(S)}{A_i} \qquad \text{(A. 11)}$$

The damage in the fabric is measured via Eqn. (A. 12) according to the maximum stretch.

$$\alpha_i = \min\left(1, \quad \alpha_i^{hist}, \quad \frac{e^{-\beta\left(\mu_i \max - \mu_i crit\right)} - e^{-0.03\beta}}{1 - e^{-0.03\beta}}\right) \tag{A. 12}$$

The damage parameter is determined by the maximum local stretch of the yarns. The maximum stretch means either the current maximum stretch or the history maximum stretch, whichever the larger one.